

ULTIMATE deblending I. A 50-band UV-to-MIR photometric catalog combining space- and ground-based data in the JWST/PRIMER survey

HANWEN SUN,^{1,2} TAO WANG,^{1,2} KE XU,^{1,2} DAVID ELBAZ,³ EMILIANO MERLIN,⁴ CHENG CHENG,⁵ EMANUELE DADDI,³ SHUOWEN JIN,^{6,7} WEI-HAO WANG,⁸ LONGYUE CHEN,^{1,2} ADRIANO FONTANA,⁴ ZHEN-KAI GAO,^{8,9} JIASHENG HUANG,⁵ BENJAMIN MAGNELLI,³ VALENTINA SANGALLI,³ YIJUN WANG,^{1,2} TIANCHENG YANG,^{1,2} YUHENG ZHANG,^{1,2} AND LUWENJIA ZHOU^{1,2}

¹*School of Astronomy and Space Science, Nanjing University, Nanjing 210093, China*

²*Key Laboratory of Modern Astronomy and Astrophysics, Nanjing University, Ministry of Education, Nanjing 210093, China*

³*Université Paris-Saclay, Université Paris Cité, CEA, CNRS, AIM, 91191, Gif-sur-Yvette, France*

⁴*INAF – Osservatorio Astronomico di Roma, Via Frascati 33, 00078 Monteporzio Catone, Rome, Italy*

⁵*Chinese Academy of Sciences South America Center for Astronomy, National Astronomical Observatories, CAS, Beijing 100101, People's Republic of China*

⁶*Cosmic Dawn Center (DAWN), Denmark*

⁷*DTU-Space, Technical University of Denmark, Elektrovej 327, DK2800 Kgs. Lyngby, Denmark*

⁸*Academia Sinica Institute of Astronomy and Astrophysics (ASIAA), No. 1, Section 4, Roosevelt Rd., Taipei 10617, Taiwan*

⁹*Graduate Institute of Astronomy, National Central University, 300 Zhongda Road, Zhongli, Taoyuan 32001, Taiwan*

(Received March 6, 2026)

Submitted to ApJS

ABSTRACT

Our understanding of the early Universe has long been limited by biased galaxy samples selected through various color criteria. With deep JWST infrared imaging, mass-complete galaxy samples can now be studied up to $z \sim 8$ for the first time. However, recent work has revealed systematic uncertainties in measuring physical properties of galaxies based solely on JWST/NIRCam and HST photometry, due to their limited wavelength coverage. This highlights the need for supplementary data, particularly in the rest-frame UV and near-infrared. Here we present the ULTIMATE-deblending project, which will eventually deliver self-consistent UV-to-Radio photometry for galaxies detected in deep JWST surveys, including both NIRCam and MIRI data. In this first paper, we release a 50-band photometric catalog spanning CFHT/U to JWST/MIRI F1800W, covering a total of 627.1 arcmin² across two JWST/PRIMER fields. We detail the reduction of JWST imaging data, the photometric procedures, and the SED-fitting methodology used to derive galaxy properties. Compared with photometry including only HST and JWST bands, the inclusion of deblended low-resolution photometry from ground-based telescopes improves the accuracy of photometric redshifts by $\sim 40\%$, while reducing the outlier fraction by $\sim 60\%$. This galaxy sample can serve as a key reference for statistical studies of galaxy formation and evolution in the early universe. All catalogs and JWST mosaics from the ULTIMATE-deblending project will be made publicly available.

Keywords: Catalogs(205); Galaxies(573); High-redshift galaxies(734); Galaxy photometry(611)

1. INTRODUCTION

Deep blank-field surveys have transformed our understanding of galaxy formation and evolution by providing unbiased selections of galaxies in the distant universe. Before the launch of the James Webb Space Tele-

scope (JWST), deep surveys based on HST (e.g., the CANDELS survey, A. Galametz et al. 2013; H. Nayyeri et al. 2017) or ground-based telescopes (e.g., the UltraVISTA survey, H. J. McCracken et al. 2012) can only provide unbiased mass-complete censuses at $z < 3$ and $\log(M_*/M_\odot) > 9$. At $z > 3$, presence of a significant population of massive old and/or dusty galaxies that are HST-dark or near-infrared (NIR)-dark (J.-S.

Huang et al. 2011; M. Franco et al. 2018; T. Wang et al. 2019; Y. Yamaguchi et al. 2019) requires deep imaging at longer wavelengths to obtain a mass-complete sample of galaxies. Meanwhile, imaging data with higher resolution is also required considering the high rate of foreground contaminants toward high-redshift galaxies (W. Liu & L. Jiang 2026). Recently, JWST has led us into a new era of extragalactic astronomy, opening rest-frame NIR windows on galaxies at $z > 3$ with unprecedented depth and resolution. With large JWST programs such as PRIMER (J. S. Dunlop et al. 2021), CEERS (S. L. Finkelstein et al. 2023), JADES (D. J. Eisenstein et al. 2026), UNCOVER (R. Bezanson et al. 2024), and COSMOS-Web (C. M. Casey et al. 2023), mass-complete samples of high-redshift galaxies have been systematically obtained and analyzed (e.g. C. Papovich et al. 2023; J. S. Kartaltepe et al. 2023; G. Yang et al. 2023; A. Weibel et al. 2024; M. Shuntov et al. 2025) (mostly) based on catalogs incorporating JWST/NIRCam and HST data (e.g. E. Merlin et al. 2024). In addition to extending the selection of a mass-complete sample of normal galaxies to higher redshifts, JWST observations also help to reveal new galaxy populations, most notably the Little Red Dots (LRDs) (e.g. P. G. Pérez-González et al. 2024; D. D. Kocevski et al. 2025; I. Labbe et al. 2025).

However, JWST surveys themselves have limited wavelength coverage, mostly focused on the NIR bands. Without comprehensive multi-band constraints on galaxy spectral energy distributions (SEDs) from rest-frame Ultraviolet (UV) to far-infrared (FIR and radio), the estimate of photometric redshifts and physical properties of galaxies from JWST surveys remain highly uncertain (J. Song et al. 2023; B. Wang et al. 2024; T. Wang et al. 2025). In rare cases, the most obscured galaxies at $z \gtrsim 6$ may still be missed in deep JWST/NIR surveys (F. Sun et al. 2025). A key challenge in combining the multi-band data from different telescopes is their different angular resolutions, ranging from ~ 0.04 arcseconds of JWST/NIRCam to ~ 40 arcseconds of Herschel/SPIRE. The ASTRODEEP team has developed a deblending framework with template-fitting photometry using high-resolution HST data as priors (E. Merlin et al. 2015, 2016a), and has applied it to self-consistently combine HST and ground-based data in the GOODS-South field (E. Merlin et al. 2021) and the Frontier Fields survey around local galaxy clusters (J. Lotz et al. 2014; A. M. Koekemoer et al. 2014; E. Merlin et al. 2016b; M. Di Criscienzo et al. 2017). Moreover, the super-deblending FIR photometry in GOODS-North (D. Liu et al. 2018) and COSMOS (S. Jin et al. 2018) has also proven the great potential of template-

fitting multiband photometry in revealing the blended fluxes at the low-resolution FIR to Radio bands. To fully exploit the new JWST datasets, it is therefore essential to perform deblending photometry from UV to radio for a mass-complete sample of JWST-detected galaxies.

Among the recent JWST surveys, the PRIMER survey (J. S. Dunlop et al. 2021) has provided one of the deepest JWST data sets with the largest survey area in the PRIMER-COSMOS and PRIMER-UDS deep fields. In particular, the deep and homogeneous JWST/MIRI coverage in the two PRIMER fields has been proven to be essential for robust stellar mass constraints of massive galaxies in the early universe (T. Wang et al. 2025). In addition to JWST, both PRIMER fields are covered by abundant multi-wavelength data collected from a number of deep surveys in the last decade, including CFHT (W.-H. Wang et al. 2022), Subaru (H. Aihara et al. 2022), Magellan (C. M. S. Straatman et al. 2016), VISTA (H. J. McCracken et al. 2012), UKIRT (Almaini et al., Hartley et al., in preparation), Spitzer (C. L. Steinhardt et al. 2014; V. Mehta et al. 2018), Herschel, SCUBA-2 (W.-H. Wang et al. 2017; Z.-K. Gao et al. 2024), VLA (V. Smolčić et al. 2017) and MeerKAT (C. L. Hale et al. 2025). These rich multi-wavelength data, combined with the new JWST observations, provide a comprehensive sampling of galaxy SEDs from UV to Radio. This enables accurate constraints on their physical properties, including stellar masses, star formation rates traced by both UV and infrared emission, and emission lines strengths inferred from narrow- and medium-band data.

Here we present the ULTIMATE-deblending project, which will eventually provide photometric catalogs across UV to Radio for JWST deep fields (starting with the two PRIMER fields). In this first paper of the ULTIMATE-deblending project, we present the reduction of JWST data in the two PRIMER fields and the construction of the UV to MIR catalog, which combines the high-resolution HST and JWST/NIRCam data with the low-resolution data from JWST/MIRI, Spitzer/IRAC, and ground-based surveys deblended using the template-fitting technique developed by the ASTRODEEP team (E. Merlin et al. 2015, 2016a). These additional data from low-resolution bands can help to improve the accuracy of photometric redshifts by providing additional wavelength coverage in UV to optical and additional narrow- and medium-bands that emphasize the breaks and emission lines. All JWST mosaics and the multi-wavelength catalog presented in this paper will be publicly released on 106.14.163.220/ultimate/ once this paper is accepted.

In future works of the ULTIMATE-deblending project, we will present the deblended FIR to Radio catalog in the two PRIMER fields (H.Sun et al., in prep) and then extend our project to other JWST deep fields. We aim to present state-of-the-art catalogs with the most complete wavelength coverage to deliver accurate photometric redshifts and physical properties constrained by the full UV to Radio SED fitting. These catalogs will directly provide robust abundance and properties of massive galaxies up to $z \sim 8.5$, enabling accurate studies of galaxy formation and evolution in the early universe. Moreover, this accurate and mass-complete reference sample of high redshift galaxies bears potential application with machine-learning algorithms (D. Masters et al. 2015; A. H. Wright et al. 2020; W. Roster et al. 2025; Z. Wang et al. 2025) to improve the modeling of galaxies in surveys with fewer bands or lower depth, such as the Euclid survey (Euclid Collaboration et al. 2025) with shallower data but a much larger point-of-view than JWST.

This paper is organized as follows: Section 2 lists the UV to MIR data set collected in our work and the reduction of JWST data; Section 3 presents the methods for source detection and multi-wavelength photometry; Section 4 shows the details of SED fitting, which is used to derive photometric redshifts and physical properties; Section 5 discusses that the low-resolution ground-based data can significantly improve the accuracy of photometric redshifts. All magnitudes presented in this paper are given in the AB system (J. B. Oke & J. E. Gunn 1983). We assume the cosmological model with $H_0=70 \text{ km} \cdot \text{s}^{-1} \cdot \text{Mpc}^{-1}$, $\Omega_m = 0.3$ and $\Omega_\Lambda = 0.7$, and adopt a P. Kroupa (2001) initial mass function during SED fitting.

2. DATA

2.1. Overview of the included data

This work focuses on the PRIMER-COSMOS and PRIMER-UDS fields. These two fields are covered by the deep JWST/NIRCam and MIRI observations from the Public Release IMaging for Extragalactic Research (PRIMER, J. S. Dunlop et al. 2021) survey. Moreover, we further collect most of the available data in these two fields, including 50 bands from UV to MIR, to construct the multi-wavelength photometric catalog. Figure 1 presents the coverage of our survey, which covers 287.3 arcmin² area in PRIMER-COSMOS and 339.8 arcmin² area in PRIMER-UDS with the combined JWST dataset shown in Section 2.1.1. Figure 2 presents the 3σ depth of point sources for all 50 bands used by our work, and the detailed depth, area, and effective wavelength are listed in Table 1.

2.1.1. JWST data

The PRIMER survey (J. S. Dunlop et al. 2021) provides large and deep JWST/NIRCam (F090W, F115W, F150W, F200W, F277W, F356W, F410M, and F444W) and MIRI (F770W and F1800W) data for PRIMER-COSMOS and PRIMER-UDS. Additionally, we also collect JWST data from many other surveys that overlap with PRIMER-COSMOS or PRIMER-UDS: the COSMOS-Web survey (C. M. Casey et al. 2023) provides more exposures for the entire PRIMER-COSMOS field with F115W, F150W, F277W, F444W, and F770W (partly covered); the JWST Emission Line Survey (JELS, K. J. Duncan et al. 2025) provides narrow-band observations (F212N, F466N, and F470N) in the central 63 arcmin² area of PRIMER-COSMOS; the PANORAMIC survey (C. C. Williams et al. 2025) and the BEACON survey (T. Morishita et al. 2025) provide additional NIRCam imaging data for both PRIMER-COSMOS and PRIMER-UDS; the JWST project GO1840 (J. Alvarez-Marquez et al. 2021) provides medium bands (F250M and F335M) observations for two pointings in PRIMER-COSMOS. All of these JWST data are reduced by our modified JWST pipeline (Section 2.2), and more JWST data observed after March 2025 will be added in a future data release.

2.1.2. Archival UV-to-MIR data

Both PRIMER-COSMOS and PRIMER-UDS have been observed with HST/WFC3 (F125W and F160W) and ACS (F606W and F814W) as part of the Cosmic Assembly Near-infrared Deep Extragalactic Legacy Survey (CANDELS, A. Galametz et al. 2013; H. Nayyeri et al. 2017). We use the HST mosaics from The DAWN JWST Archive (DJA, v7.0), which additionally combines the HST data from the Cosmic Evolution Survey (N. Scoville et al. 2007) and the UVCANDELS survey (V. Mehta et al. 2024).

Apart from the high-resolution data from JWST and HST, multi-band data from ground-based telescopes and Spitzer are also used by our catalog with deblending photometry (Section 3.4), including the u^* -band data taken with CFHT from the MegaCam Ultra-deep Survey (MUSUBI, W.-H. Wang et al. 2022); eight bands (g , r , i , z , y , NB816, NB921, and NB1010) from the third data release of the Hyper Suprime-Cam Subaru Strategic Program (H. Aihara et al. 2022); five medium bands (Magellan/Fourstar J1, J2, J3, H1, and Hs) taken with the ZFOURGE survey (C. M. S. Straatman et al. 2016), which covers half of both PRIMER-COSMOS and PRIMER-UDS; NIR images (Y , NB118, J , H , and K_s) for PRIMER-COSMOS from the fifth data release of the UltraVISTA near-infrared imaging survey (H. J.

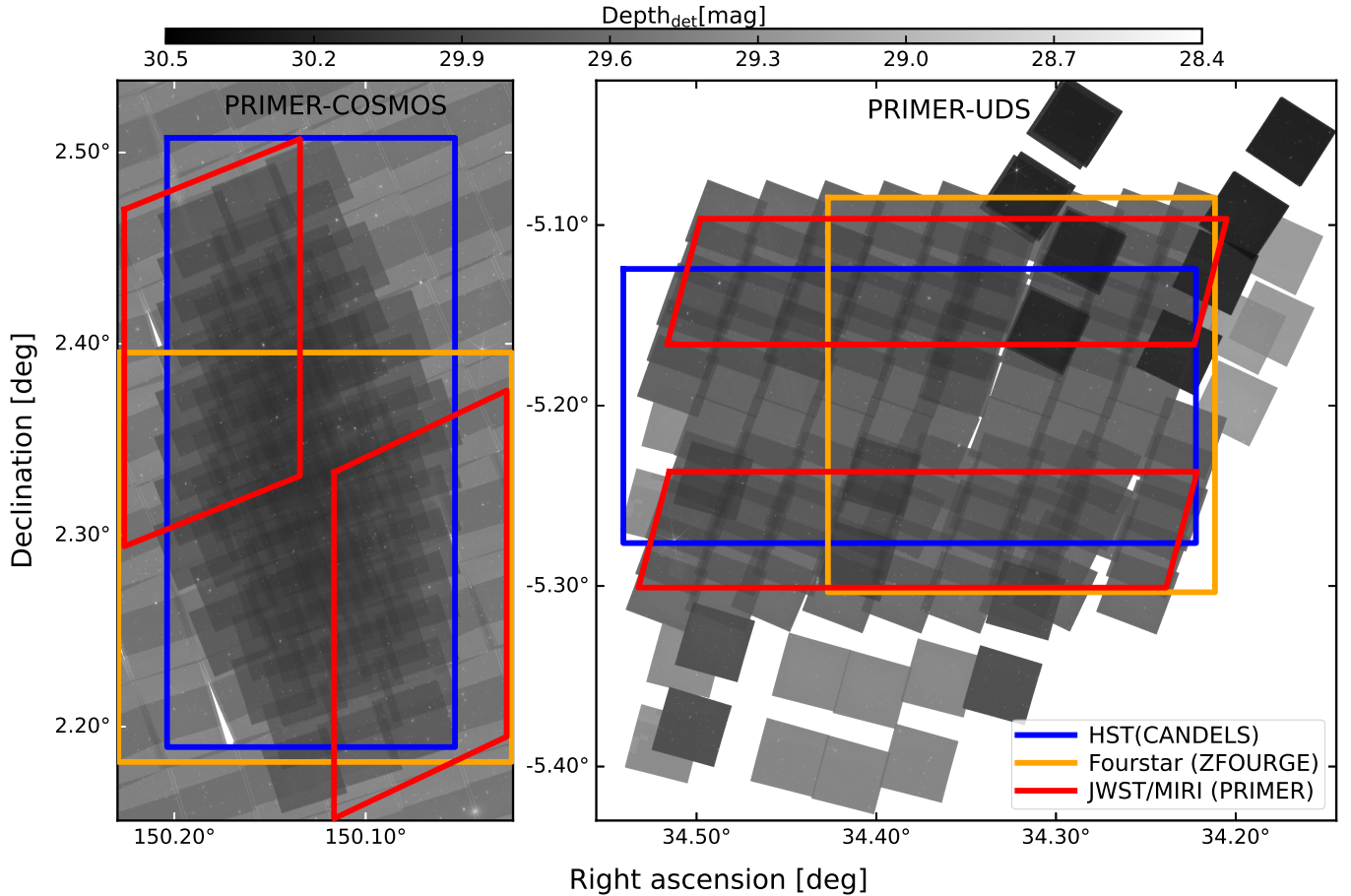


Figure 1. The coverage of the key surveys within **PRIMER-COSMOS** (left panel) and **PRIMER-UDS** (right panel). The background grayscale image presents the 3σ limiting depth (in $0.2''$ diameter apertures) for point sources of the stacked JWST/NIRCam image, which is used for source detection. The blue, orange, and red lines show the coverage of the HST data from the CANDELS survey (A. Galametz et al. 2013; H. Nayyeri et al. 2017), the Magellan/Fourstar medium-bands data from the ZFOURGE survey (C. M. S. Straatman et al. 2016), and the JWST/MIRI data taken with the PRIMER survey. The boundary of our mosaics in PRIMER-COSMOS is determined by the coverage of the JWST/MIRI data from PRIMER (J. S. Dunlop et al. 2021) and the deep SCUBA-2 data from STUDIES (W.-H. Wang et al. 2017; Z.-K. Gao et al. 2024).

McCracken et al. 2012); NIR images (J , H , and K) for PRIMER-UDS from the UKIDSS Ultra-Deep Survey data release 11 (Almaini et al., Hartley et al., in preparation); and the Spitzer/IRAC $5.8\ \mu\text{m}$ and $8.0\ \mu\text{m}$ mosaics reduced by the SPLASH team (C. L. Steinhardt et al. 2014; V. Mehta et al. 2018), which was observed as part of the S-COSMOS (D. B. Sanders et al. 2007) and SpUDS (SpUDS Team 2020) survey.

2.2. Reduction of JWST data

The reduction of all JWST imaging data is performed using our modified version of the JWST Calibration Pipeline. Data collected before August 2024 are reduced using the JWST Calibration Pipeline v1.13.4 (H. Bushouse et al. 2024) with the Calibration Reference Data System (CRDS) pipeline mapping 1241, while data collected after August 2024 are reduced using the JWST Calibration Pipeline v1.19.1 (H. Bushouse et al. 2025)

with the CRDS pipeline mapping 1413. We have tested that different versions of the JWST Calibration Pipeline would not yield any systematic bias in photometric results, and the mosaics reduced by our modified pipeline based on these two versions have comparable quality. Therefore, we decided to keep the old mosaics reduced by the JWST Calibration Pipeline v1.13.4.

For JWST/NIRCam images, we first run the default stage 1 pipeline to perform Detector-level corrections, during which we set “jump.expand_large_events = True” and increased the expand factor to mask the “snowballs”¹⁰ around large cosmic ray events. Based on the output of stage 1 (i.e. *_rate.fits), we further subtract

¹⁰ Description of snowballs can be found at jwst-docs.stsci.edu/known-issues-with-jwst-data/shower-and-snowball-artifacts.

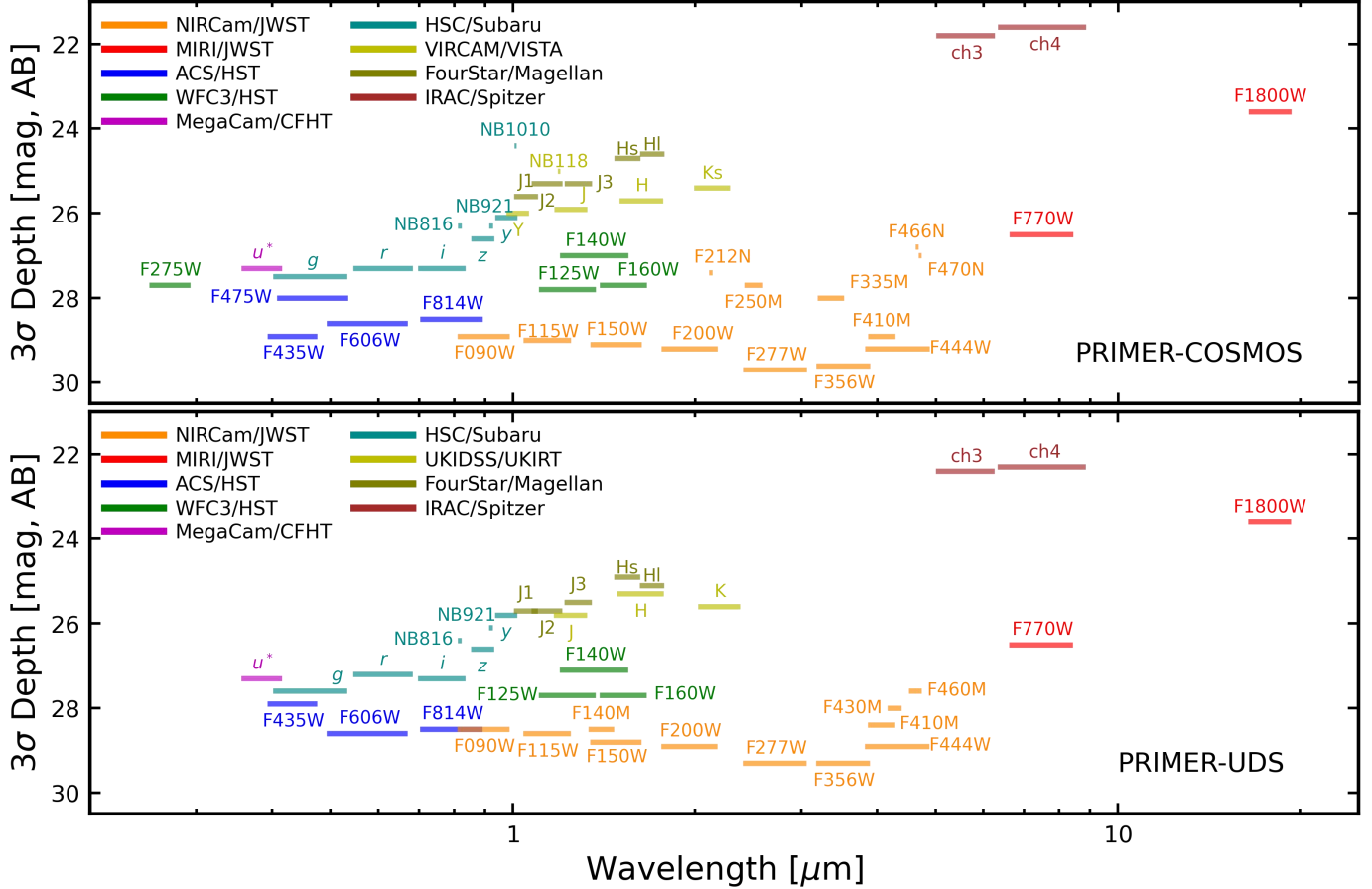


Figure 2. The 3σ depth and wavelength range of the multi-band data used by PRIMER-COSMOS (upper panel) and PRIMER-UDS (lower panel). All depths of point sources are measured using empty circular apertures and have been corrected to consider the aperture losses. We use the apertures with the highest sensitivity (among $0.2''$, $0.5''$, and Kron apertures) for JWST and HST data, and apertures with $d = 3.5 \times \text{FWHM}_{\text{PSF}}$ for the other low-resolution data.

the scattered light (“claws” and “wisps”) using the templates provided by the JWST User Documentation¹¹. In addition to this correction, we also adopt the methods given by K. J. Duncan et al. (2025) to subtract or mask the unstable wisps that vary between different pointings.

Stage 2 of the JWST Calibration Pipeline performs the Instrument-level calibrations for individual exposures. After running the default stage 2 pipeline, we further run a set of additional calibrations for the output “cal” files: Firstly, we subtract the background and detect sources from each individual exposure using photutils v1.5.0 (L. Bradley et al. 2022). In order to accurately mask the extended structures of bright sources before the subtraction of stripes while avoiding masking the noise, we set a relatively high detection threshold and then extended the range of each detected bright source

by 2 arcseconds on the segmentation map, which is then used for masking of sources. Secondly, following M. B. Bagley et al. (2023), we remove the stripe-like $1/f$ noise by subtracting a median value for each row and column in each amplifier. For some exposures from PRIMER-UDS, we also subtract the slanted stripes by fitting them with cubic polynomials. Thirdly, we identify the remaining cosmic rays and hot pixels (e.g. M. J. Rieke et al. 2023) with their sharper edges compared to the point sources and set the DQ values of the affected pixels as 1 (so they can be ignored by the pipeline). Lastly, we visually identify and mask the remaining noise structures on the image, such as the “Dragon’s Breath”¹² and the trajectory of nearby celestial bodies.

Stage 3 of the JWST Calibration Pipeline combines all available single exposures in one field into a large

¹¹ The templates of claws and wisps provided by the JWST user documentation are available at stsci.app.box.com/s/1bymvfl1krqbdn9rnkluzqk30e8o2bne.

¹² Description of the “Dragon’s Breath” can be found at jwst-docs.stsci.edu/known-issues-with-jwst-data/nircam-known-issues/nircam-scattered-light-artifacts.

Table 1. UV to MIR data used in the photometric catalog

Instrument /Telescope	Band	λ_{eff} [Å]	Bandwidth ^a [Å]	Depth ^b _{COS} (mag)	Area _{COS} (arcmin ²)	Depth ^b _{UDS} (mag)	Area _{UDS} (arcmin ²)	FWHM (")
NIRCam /JWST	F090W	8985	1773	28.9/27.9/27.1 ^c	146.2	28.5/27.5/26.8	268.1	0.033
	F115W	11434	2055	29.0/28.0/27.1 ^d	287.5	28.6/27.6/26.9	282.1	0.040
	F140M	14023	1367	-	-	28.5/27.6/26.9	76.1	0.048
	F150W	14873	2890	29.1/28.1/27.3	287.2	28.8/27.8/27.1	281.8	0.050
	F200W	19680	4190	29.2/28.2/27.4	146.3	28.9/27.9/27.2	264.0	0.066
	F212N	21212	274	27.4/26.4/25.6	63.1	-	-	0.072
	F250M	25006	1783	27.7/26.9/26.1	10.1	-	-	0.085
	F277W	27279	6615	29.7/28.7/27.9	287.3	29.3/28.4/27.7	287.5	0.092
	F335M	33537	3389	28.0/27.1/26.4	10.1	-	-	0.111
	F356W	35287	7239	29.6/28.7/28.0	147.4	29.3/28.5/27.8	287.9	0.116
	F410M	40723	4263	28.9/28.1/27.5	147.4	28.4/27.8/27.2	255.9	0.137
	F430M	42784	2295	-	-	28.0/27.2/26.7	81.0	0.144
	F444W	43504	10676	29.2/28.5/27.9	286.9	28.9/28.2/27.5	287.6	0.145
	F460M	46270	2309	-	-	27.6/26.9/26.4	78.7	0.157
	F466N	46540	535	26.8/26.2/25.7	63.0	-	-	0.158
F470N	47078	510	27.0/26.4/25.8	63.0	-	-	0.160	
MIRI /JWST	F770W	75225	18278	26.5/26.4/25.8	194.3	26.5/26.4/25.8	128.7	0.269
	F1800W	178734	29146	23.1/23.6/23.6	111.2	23.0/23.6/23.6	126.9	0.591
ACS /HST	F435W	4342	822	28.9/27.9/27.2	126.8	27.9/26.9/26.3	185.2	0.08
	F475W	4709	1272	28.0/27.1/26.5	85.9	-	-	0.08
	F606W	5809	1772	28.6/27.8/27.1	225.5	28.6/27.8/27.1	192.6	0.08
	F814W	7973	1889	28.5/27.6/27.0	Full	28.5/27.6/26.9	204.7	0.09
WFC3 /HST	F275W	2720	424	27.7/26.8/26.1	87.8	-	-	0.07
	F125W	12364	2674	27.8/27.4/26.8	182.2	27.7/27.4/26.8	177.3	0.16
	F140W	13735	3570	27.0/26.6/26.1	135.5	27.1/26.7/26.2	123.1	0.17
	F160W	15278	2750	27.7/27.3/26.8	199.2	27.7/27.4/26.9	187.3	0.17
MegaCam /CFHT	<i>u</i> *	3858	598	27.3	Full	27.3	Full	0.86
HSC /Subaru	<i>g</i>	4670	1303	27.5	Full	27.6	Full	0.83
	<i>r</i>	6136	1382	27.3	Full	27.2	Full	0.77
	<i>i</i>	7657	1383	27.3	Full	27.3	Full	0.66
	NB816	8168	112	26.3	Full	26.4	Full	0.70
	<i>z</i>	8920	781	26.6	Full	26.6	Full	0.78
	NB921	9202	134	26.3	Full	26.1	Full	0.67
	<i>y</i>	9760	824	26.1	Full	25.8	Full	0.70
	NB1010	10097	97	24.4	Full	-	-	0.77
VIRCAM /VISTA	<i>Y</i>	10193	880	26.0	Full	-	-	0.82
	NB118	11907	117	25.0	Full	-	-	0.75
	<i>J</i>	12485	1554	25.9	Full	-	-	0.79
	<i>H</i>	16354	2720	25.7	Full	-	-	0.76
	<i>Ks</i>	21376	2914	25.4	Full	-	-	0.75
UKIDSS /UKIRT	<i>J</i>	12483	1590	-	-	25.8	Full	0.83
	<i>H</i>	16313	2920	-	-	25.3	Full	0.85
	<i>K</i>	22010	3510	-	-	25.6	Full	0.85
Fourstar /Magellan	<i>J1</i>	10521	956	25.6	158.3	25.7	165.9	0.59
	<i>J2</i>	11407	1330	25.3	155.5	25.7	160.2	0.57
	<i>J3</i>	12835	1325	25.3	152.8	25.5	164.6	0.54
	<i>Hs</i>	15479	1543	24.7	153.6	24.9	161.5	0.55
	<i>Hl</i>	17001	1565	24.6	153.7	25.1	162.8	0.62
IRAC /Spitzer	<i>ch3</i>	56281	12561	21.8	Full	22.4	Full	1.9
	<i>ch4</i>	75890	25289	21.6	Full	22.3	Full	2.0

NOTE. — (a) The effective width of the filter. (b) The average 3σ depth for point sources. (c) The depths of high-resolution images are given with the 0.2", 0.5", and Kron apertures with aperture corrections. (d) For the bands with supplementary coverage from COSMOS-Web (F115W, F150W, F277W, F444W, and F770W) at the edge of the image, we only show the average depth of the area covered by the PRIMER survey.

and deep image. During the ‘‘TweakReg’’ step of stage 3, we use an astrometric reference catalog based on the HST/F160W or F814W images from the Grizli Image Release v7.0. For a few areas without any HST data, we use the positions reported by the COSMOS2020 (J. R. Weaver et al. 2022) and the FENIKS catalog (K. Zaidi et al. 2024) instead. All of these reference catalogs have been aligned with the third data release of Gaia (Gaia DR3, Gaia Collaboration et al. 2018). Figure 3 shows the results of our astrometric alignment, the astrometric scatter is $\sigma_{\text{RA}} \approx \sigma_{\text{Dec}} \approx 0.02''$ between our mosaics and Gaia DR3, and $\sigma_{\text{RA}} \approx \sigma_{\text{Dec}} \approx 0.009''$ across different NIRCcam bands. Then, we run the remaining part of stage 3 with default parameters. The pixel scales of our final mosaics are set to be $0.04''/\text{pixel}$ for JWST/NIRCcam images and $0.08''/\text{pixel}$ for JWST/MIRI images.

For JWST/MIRI images, in addition to the modifications mentioned above, we make the following improvements to the JWST Calibration Pipeline as shown in T. Wang et al. (2025). Firstly, the default flat fields provided by CRDS are replaced by the super-sky flat fields, which are constructed for each MIRI pointing by stacking the output of stage 1 from all pointing observed within 5 days. Secondly, we perform the source masking for MIRI images in an iterative way: we first construct the flat fields and run stage 2 without source masking, and then perform source masking using the output of our first iteration and repeat those operations for a second time.

3. SOURCE DETECTION AND PHOTOMETRY

3.1. PSF match

Before source detection, we perform point spread function (PSF) matches to ensure that all images used for detection have the same resolution. To get the effective PSF for each JWST and HST filter, we stack $4'' \times 4''$ cutouts of point sources from our real mosaics. These point sources are selected as the sources with the highest fraction of flux density within a small ($d = 0.2''$) aperture ($f_{0.2''}/f_{4''}$). The fluxes outside the $4'' \times 4''$ cutouts are corrected using the model PSFs from the Python package Webbpsf v1.1.1 (M. D. Perrin et al. 2015; S. Osborne et al. 2018), whose enclosed energy should only be inaccurate in the center (Z. Ji et al. 2024).

For all HST and JWST images whose resolutions are better than the JWST/NIRCcam F444W image, we use photutils v1.5.0 (L. Bradley et al. 2022) with the CosineBellWindow to obtain the convolution kernels that match their effective PSF to that of F444W. The convolution is performed using the ‘‘convolve_fft’’ function from Astropy v5.0 (Astropy Collaboration et al.

2022). Based on this convolution, source detection will be performed at the F444W resolution (Section 3.2). We do not perform PSF match for the JWST/NIRCcam F410M, F430M, F460M, F466N, and F470N images because their resolutions are already comparable (difference of PSF FWHM within 10%) to F444W. And the larger PSFs of HST/WFC3 mosaics are considered using an additional correction during aperture photometry (Section 3.3).

3.2. ‘‘Cold’’ and ‘‘hot’’ dual mode detection

After the PSF match, we make an inverse-variance-weighted stack of six JWST/NIRCcam longwave (LW) images (F277W, F356W, F410M, F430M, F444W, and F460M) as the detection image. The stacking of all LW images enables the deepest detection for the average sample of galaxies. A few faint and red galaxies may have lower SNR in these stacks than they would in individual filters, but they would likely be detected only in one or two bands and their photometric redshifts and physical properties cannot be constrained. All saturated stars on this detection image are visually identified and filled so that they can be detected as one single star in our catalog. Then, we perform source detection by running Source-Extractor v2.25.0 (E. Bertin & S. Arnouts 1996) in dual ‘‘cold’’ and ‘‘hot’’ modes to reach the limiting depth of the detection image without over-splitting the bright sources (e.g. A. Galametz et al. 2013; Y. Guo et al. 2013). This is necessary for our deblending photometry, which requires accurate measurement of the bright sources to reduce the flux contamination caused by them. The key parameters for the dual modes detection are listed in Table 2. Firstly, we run cold mode detection to detect 20059 and 28017 bright sources in PRIMER-COSMOS and PRIMER-UDS, respectively. Then, 138609 (176214) faint sources are detected by the hot mode in PRIMER-COSMOS (UDS). Lastly, we exclude all hot-mode sources that are located within the Kron aperture of a cold-mode source and reallocate the corresponding pixels on the segmentation map to this cold-mode source. After this exclusion, our final catalog consists of 135855 and 172384 sources in PRIMER-COSMOS and PRIMER-UDS, respectively.

The number count density of our catalog as a function of F444W magnitude is shown in Figure 4, which is consistent with the JWST Advanced Deep Extragalactic Survey (JADES) (D. J. Eisenstein et al. 2026) at the bright end. Since the JWST mosaics from JADES are much deeper than PRIMER, the detection completeness of our work can be inferred from the number count density ratio between our catalog and the JADES cata-

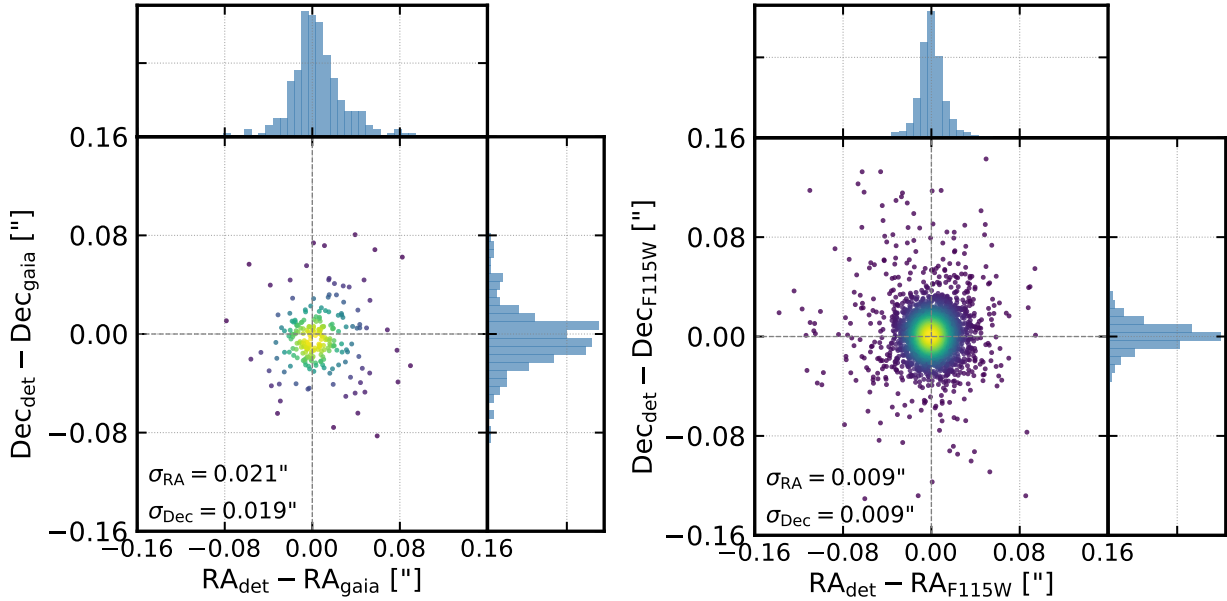


Figure 3. Validation of our astrometric alignment. The left panel shows the astrometric difference between our detection image and Gaia DR3 (Gaia Collaboration et al. 2018), while the right panels shows the astrometric difference between different NIRCcam bands. Sources from both PRIMER-COSMOS and PRIMER-UDS are included in this figure. Outliers in the right panel include galaxies with different morphologies at different bands.

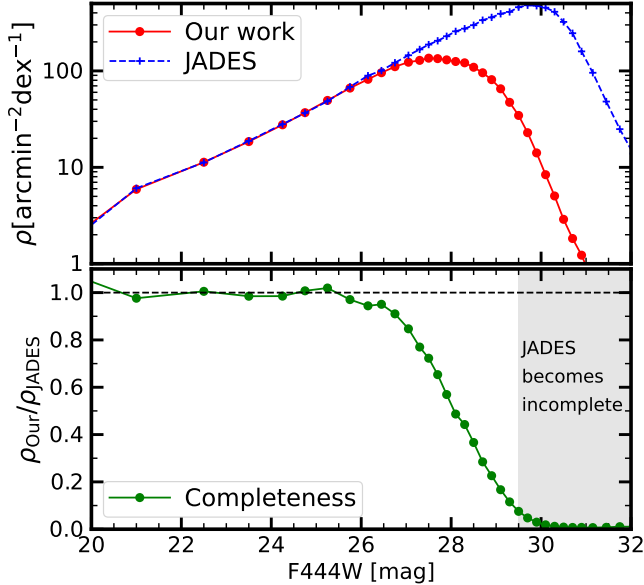


Figure 4. Source number counts and detection completeness. The red line in the upper panel presents the source number count density as a function of F444W magnitude. The blue line shows the number count density from the JADES survey (D. J. Eisenstein et al. 2026). The lower panel shows the ratio between the number count density of our work and JADES, which presents the detection completeness of our catalog.

log. According to this ratio, our catalog reaches $\sim 80\%$ (50%) completeness at $\text{mag}_{444} \sim 27.2$ (28.2).

3.3. Aperture photometry for high-resolution data

For high-resolution images from JWST/NIRCcam and HST, we perform aperture photometry with the software APHOT (E. Merlin et al. 2019) using circular apertures within diameters $0.2''$, $0.3''$, $0.4''$, $0.5''$, $0.7''$, and $1.0''$ as well as a Kron elliptical aperture with the Kron parameter $k = 2.5$ (R. G. Kron 1980). The Kron apertures are calculated by Source-Extractor on the detection image, and then imported by APHOT. During the aperture photometry, APHOT replaces the bad pixels or the pixels belonging to another source on the segmentation map with the pixels symmetric with respect to the centroid of the source. A local background estimation is also computed and then subtracted by APHOT. If the resolution of the measurement band is better or comparable to that of F444W (as seen in HST/ACS and JWST/NIRCcam images), the flux densities are measured on the PSF-matched images (Section 3.1) with the same resolution. Conversely, for HST/WFC3 images, we convolve the stacked detection image (Section 3.2) to match their PSF. Then, we use the ratio $f_{\text{det, before convolution}}/f_{\text{det, after convolution}}$ of each source to correct the additional aperture loss due to the lower resolution of HST/WFC3. We determine the error of all aperture fluxes using the root-mean-square (RMS) value of 1000 empty apertures for each band and each aperture size. Then, the uncertainties of flux densities estimated by APHOT are multiplied by the ratio between this RMS and the median uncertainty in the catalog.

Table 2. Key parameters of SExtractor in cold and hot modes detection

	Cold mode	Hot mode
DETECT_MINAREA	10	5
DETECT_THRESH	18.0 (16.0) ^a	1.5
FILTER_NAME	gauss_5.0_9x9.conv	gauss_4.0_7x7.conv
DEBLEND_NTHRESH	64	64
DEBLEND_MINCONT	0.0006	0.0001
BACK_SIZE	200	72
BACK_FILTERSIZE	3	3
WEIGHT_TYPE	MAP_RMS	MAP_RMS

NOTE. — (a) Since the NIRCcam observations for Primer_COSMOS are deeper than Primer_UDS, different cold mode detection thresholds are used for these two fields (18.0 for Primer_COSMOS and 16.0 for Primer_UDS).

To obtain the total flux densities, we perform the aperture correction as follows: Firstly, we correct the aperture losses of flux densities measured by Kron apertures, which is necessary since the PSFs of JWST have nonnegligible contributions ($\gtrsim 10\%$) from the outskirts. For faint and compact sources whose Kron apertures are smaller than the Kron aperture calculated for the PSF, the flux losses outside their Kron apertures are determined by measuring the ratio of the PSF outside these apertures ($1 - f_{\text{Kron}(\text{source}),\text{PSF}}/f_{\text{tot,PSF}}$). For the other sources with larger Kron apertures, we directly use the fraction of flux density outside the Kron aperture calculated for the PSF ($1 - f_{\text{Kron}(\text{PSF}),\text{PSF}}/f_{\text{tot,PSF}}$, $\sim 10\%$ for NIRCcam) to avoid underestimating the aperture loss for these bright and extended sources. We note that the Kron apertures of some sources can be unreliable due to the enhanced background structure (e.g. [M. J. Rieke et al. 2023](#)) or low SNR. These unreliable Kron apertures are identified using the empirical criteria

$$\left\{ \begin{array}{l} \text{SNR}_{\text{Kron,det}} < 3 \\ \text{or } (A > 2 \wedge f_{\text{area}} > 18 \wedge f_{\text{flux}} > 6) \\ \text{or } (A > 5 \wedge f_{\text{area}} > 6 \wedge f_{\text{flux}} > 2) \end{array} \right. \quad (1)$$

where A is the profile RMS along the major axis of each source ("A_image" from source-extractor), $f_{\text{area}} \equiv \text{area}(\text{Kron})/\text{area}(\text{seg})$ is the ratio of the area of Kron aperture and segmentation, $f_{\text{flux}} \equiv \text{flux}(\text{Kron})/\text{flux}(\text{seg})$ is the ratio of the flux density within Kron aperture and segmentation. Once the Kron aperture of a source is considered to be unreliable, we set "flag_kron = 1" in the catalog. Then, for flux densities measured by circular apertures, we correct them to total fluxes using $f_{\text{aper,measure}} \times f_{\text{Kron,det}}/f_{\text{aper,det}}$, where $f_{\text{aper,measure}}$ and $f_{\text{aper,det}}$ are the flux density measured by each of the circular aperture in the measurement and detection band, respectively. If a source has "flag_kron = 1", we adopt the point source assumption to correct the aperture loss of circular apertures instead.

Lastly, among the seven apertures (0.2", 0.3", 0.4", 0.5", 0.7", 1.0", and Kron), we choose the best aperture for each source. If a source has $\text{SNR}_{\text{Kron,det}} > 20$ and is not selected by Equation 1, we use the Kron aperture as the best aperture. Otherwise, we choose the aperture with the largest $\text{SNR}_{\text{aper,det}} \times f_{\text{aper,det}}/f_{\text{Kron,det}}$ (when $f_{\text{aper,det}}/f_{\text{Kron,det}}$ is smaller, the aperture correction can be more uncertain). This best aperture is then used for all HST and JWST/NIRCcam bands since the PSFs of all these bands are smaller than our smallest circular aperture with $d=0.2$ ".

3.4. TPHOT deblending photometry for low-resolution data

For the data from JWST/MIRI, ground-based telescopes (CFHT, Subaru, VISTA, UKIRT, Megellan), and Spitzer/IRAC, we perform deblending photometry with the software TPHOT v2.0 ([E. Merlin et al. 2015, 2016a](#)). We use the image of the closest JWST/NIRCcam band as the high-resolution prior for TPHOT photometry. Then, TPHOT convolves the high-resolution prior to matching the PSF of the measurement band, and fits the fluxes in the measurement band with these convolved high-resolution priors until the linear χ^2 solution is obtained. During TPHOT photometry, we exclude the faint sources with $\text{SNR} < 3$ on the closest JWST image to avoid unreliable high-resolution priors, and then fit all remaining sources with the cells-on-objects algorithm to split the large mosaic into smaller cells ([E. Merlin et al. 2015](#)). The flux priors of all fitted sources are taken as their flux densities at the closest JWST band, and we input relatively large uncertainties of flux priors to TPHOT so that the output flux densities will not be biased by flux prioring. During the second pass of TPHOT fitting, we allow shifting of the positions of sources up to 0.3" to account for astrometric differences (Although most of the low-resolution mosaics have also been aligned with Gaia, their astrometric accuracy can be poorer due to lower resolution). Figure 5 shows an

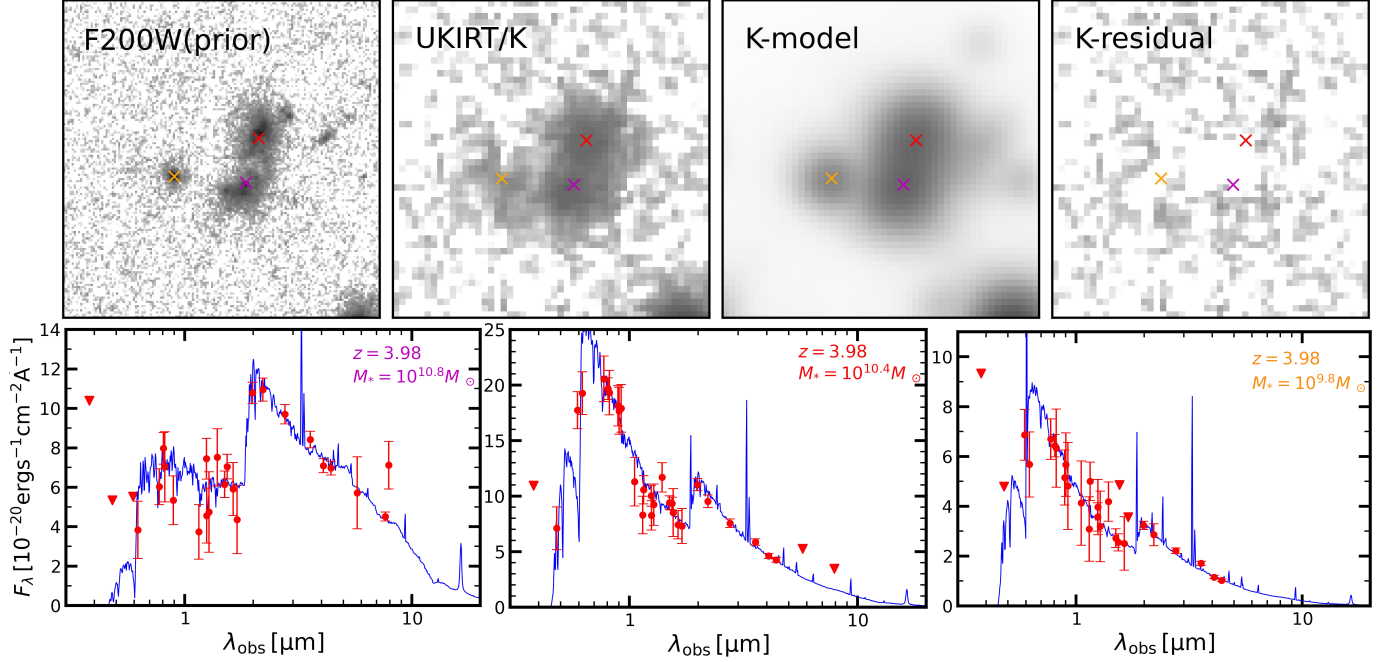


Figure 5. Example of the TPHOT deblending photometry. The upper panels show the images in the center of the Bigfoot protocluster in PRIMER-UDS (H. Sun et al. 2025), with locations of the three massive member galaxies in Bigfoot marked as crosses. The first image is the high-resolution image from JWST/NIRCam F200W, which is used to provide high-resolution priors for K-band photometry. The second image is the low-resolution image from UKIRT/K, which is the measurement band in this example. The third and fourth images are the best-fit models and residuals after the deblending photometry. The lower panels show the best-fit SEDs (combining both high-resolution and low-resolution data) of three member galaxies in Bigfoot from Bagpipes.

example of deblending photometry in the central area of the Bigfoot protocluster at $z = 3.98$ in PRIMER-UDS (H. Sun et al. 2025). We show that even in the core of a protocluster, one of the densest areas in the universe, we are still able to obtain reliable SEDs with the deblending photometry.

To provide the uncertainties of flux densities measured by TPHOT, we put 1000 empty apertures whose diameter is 3.5 times larger than the FWHM of the PSF of each low-resolution band in the residual map after TPHOT photometry. This factor 3.5 was calibrated using the results of simulated photometry for sources with known fluxes in six bands (CFHT/U; Subaru/B, IB427, and NB2300; UltraVISTA/J, and Ks) during our previous work targeting protocluster J1001 (H. Sun et al. 2024). Then, we use the RMS values of flux densities measured by these empty apertures divided by the median flux uncertainty output by TPHOT as the correction factor for the flux uncertainties of all sources output by TPHOT. As an example to prove the reliability of the above procedure, we present the results of simulated photometry for point sources with the updated UltraVISTA/Ks band data used by this work (which is 0.7 magnitude deeper than the Ks band data of J1001) in Figure 6. At each input magnitude, we inject 500 point

sources into the residual map and run TPHOT photometry for them. The SNR of these simulated point sources can then be calculated as $\text{flux}_{\text{input}}/\text{RMS}_{\text{output}}$, where $1/\text{RMS}_{\text{output}}$ is the 1σ scatter of the output flux densities of these 500 point sources. In Figure 6, the orange line shows the 95th percentile of the SNRs corrected by the empty apertures, which represents the SNRs of isolated point sources (with highest SNR at certain magnitude) in our catalog. This orange line is consistent with the SNRs of simulated point sources (the red dotted line), showing that we can use the method based on empty apertures (which is more efficient) to estimate the uncertainties of TPHOT photometry.

After TPHOT photometry, we select the unreliable flux densities measured by TPHOT as follows: Firstly, TPHOT can not properly fit the sources around bright stars, especially for bright stars saturated on either the measurement image or the JWST image used as the high-resolution prior. These sources affected by bright stars can be selected using

$$d < 50.0 - 2.5 \times R, \quad (2)$$

where d is the distance to the bright sources in arcseconds, R is the R band magnitude from Gaia DR3 (Gaia Collaboration et al. 2018), and the empirical parameters

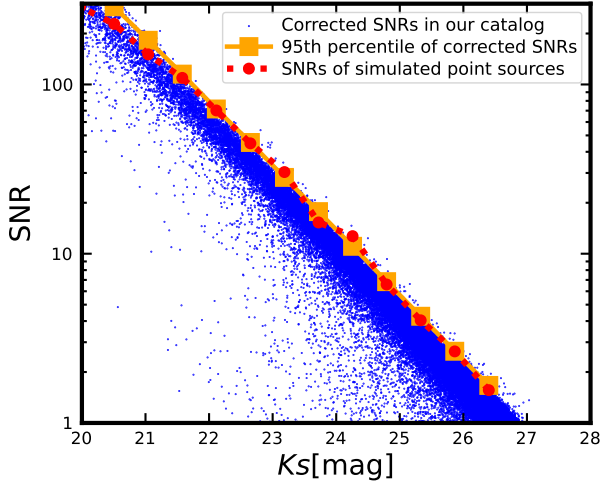


Figure 6. Example of the uncertainty of TPHOT deblending photometry in the Ks band. The blue points show the SNRs reported in our catalog, which have been corrected using 1000 empty apertures with $d = 3.5 \times \text{FWHM}_{\text{PSF}}$. The orange line shows the 95th percentile of the corrected SNRs, which represents the SNRs of point sources. The red dotted line shows the SNRs of simulated point sources, which are calculated as $\text{flux}_{\text{input}}/\text{RMS}_{\text{output}}$ from the simulated TPHOT photometry. The orange line is almost overlapping with the red dotted line, showing that the flux uncertainties corrected by empty apertures are consistent with the results of simulated photometry.

50 and 2.5 are determined by visual inspection. Sources selected by Equation 2 have “flag_TPHOT = 1” in our catalog. Secondly, we compare the flux densities from low-resolution images and high-resolution images at similar wavelengths (including four comparisons in total: i compared with F814W, z compared with F090W, J compared with F115W, and H compared with F150W). The outliers from these four comparisons can be selected using

$$|\text{mag}_h - \text{mag}_l| > -2.5 * \log\left(1 - \frac{\Sigma \sqrt{\sigma_h^2 + \sigma_l^2}}{\max(f_h, f_l)}\right) + 0.3, \quad (3)$$

where Σ is the confidence level; σ_h and σ_l are the 1σ flux uncertainty at the high-resolution band and the low-resolution band; f_h and f_l are the flux densities at the high-resolution band and the low-resolution band, respectively, and the color term 0.3 is a conservative value adopted to consider the intrinsic color between the high-resolution band and low-resolution band. Sources selected with $\Sigma = 5$ from one comparison or $\Sigma = 2.5$ from at least two comparisons are considered to have unreliable deblending results, which have “flag_TPHOT = 2” in our catalog. This can help us exclude all suspicious data, which mainly belongs to sources close to a bright and extended galaxy or close mergers. Thirdly, we se-

lect the sources close (distance $< 3''$) to the edge of our detection image, and set “flag_TPHOT = 3”.

Combining the above criteria, 25348 sources ($\sim 8.2\%$, 12880 in PRIMER-COSMOS and 12468 in PRIMER-UDS) are considered to have unreliable deblending results. For these sources, we exclude all fluxes measured by TPHOT during SED fitting. For JWST/MIRI data, if the result from TPHOT is unreliable (“flag_TPHOT > 0 ”) or has $\text{SNR}_{\text{TPHOT}} < 2$, we use the result from aperture photometry instead. The aperture photometry of JWST/MIRI is performed using the same method as HST/WFC3 (Section 3.3), but we only consider the apertures larger than the PSF of each JWST/MIRI band as the best aperture for MIRI (For example, we only use circular apertures with $d = 0.7''$, $1.0''$, and Kron apertures for F1800W).

3.5. Photometric validations

Our catalog combines flux densities measured by different photometric methods, so we validate their consistency in Figure 7. The left panel compares the flux densities from JWST/NIRCam F150W and HST/WFC3 F160W images, which are both measured by aperture photometry with APHOT but are processed with different PSF matching programs because of their different resolutions (Section 3.3). Meanwhile, the right panel compares the flux densities from JWST/NIRCam F150W and VISTA/H, which are measured by aperture photometry with APHOT and deblending photometry with TPHOT, respectively. For both comparisons, the $\sim 1.5\mu\text{m}$ flux densities measured from different telescopes using different methods are consistent with almost no systematic offset. This confirms the reliability of the combination of different photometric methods and also validates the accuracy of the photometric calibration of the imaging data. We note that the strong outliers in Figure 7 include saturated stars, sources around bright nearby sources, and sources close to the edge of the image. These unreliable sources have been selected and flagged in our catalog (see Section 3.4).

Figure 8 compares our photometric results with the archival ground-based (J. R. Weaver et al. 2022), HST-based (H. Nayyeri et al. 2017), and JWST-based (M. Shuntov et al. 2025) catalogs in PRIMER-COSMOS to further validate the reliability of our catalog. Our results do not have systematic bias with the COSMOS2020 (J. R. Weaver et al. 2022) and COSMOS2025 (M. Shuntov et al. 2025) catalogs across all magnitudes. However, the flux densities reported by the CANDELS catalog (A. Galametz et al. 2013; H. Nayyeri et al. 2017) could be systematically under-estimated because they do not consider the aperture loss of the Kron aper-

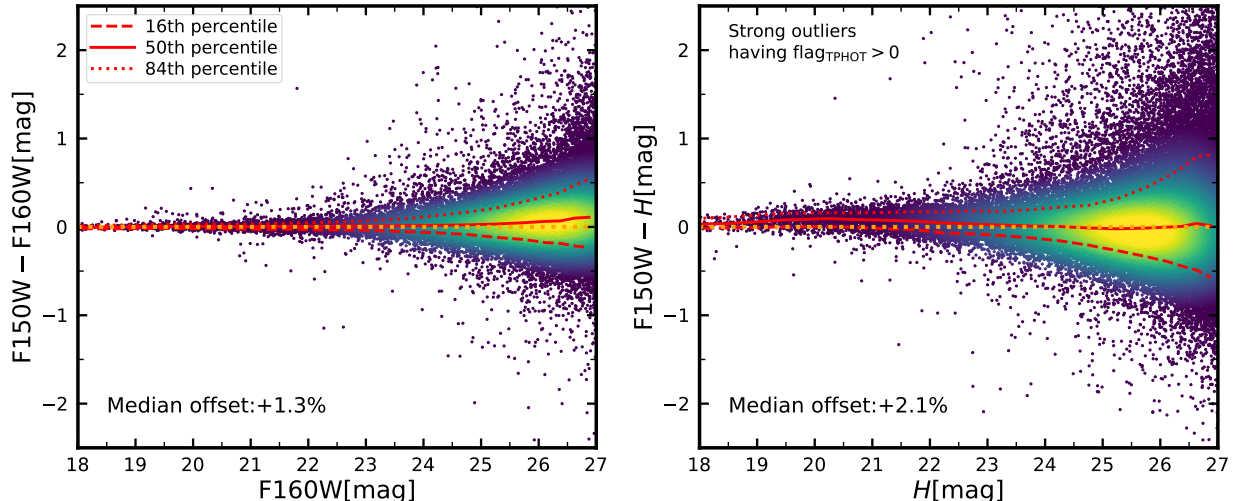


Figure 7. Comparison of $\sim 1.5\mu\text{m}$ flux densities measured from different telescopes with different methods. The left panel compares the photometric results from JWST/NIRCam F150W and HST/WFC3 F160W images, while the right panel compares the results from JWST/NIRCam F150W and VISTA/H. The red dashed, solid, and dotted lines show the 16th, 50th, and 84th percentiles of the colors as functions of magnitudes, respectively. We also report the median offset for all sources with $\text{SNR} > 7$ in both bands. These results agree well with almost no bias, and we have checked that most of the strong outliers have been selected to have $\text{flag_TPHOT} > 0$ in our catalog (see Section 3.4).

tures (especially for the faint sources with smaller Kron apertures). This problem of the CANDELS catalog has also been reported by R. E. Skelton et al. (2014). We note that the scatter between our results and COSMOS2025 can be larger because of the different mosaics used for photometry: M. Shuntov et al. (2025) only used the JWST data taken by the COSMOS-Web survey (C. M. Casey et al. 2023), while our JWST mosaics can be much deeper with the data from the PRIMER survey. We have also tested that the flux comparison between our NIRCam fluxes and that reported by the ASTRODEEP-JWST catalog (E. Merlin et al. 2024) has smaller scatters, but the NIRCam fluxes of faint sources from ASTRODEEP-JWST can also be underestimated (by $\sim 10\%$) due to the lack of aperture loss corrections for Kron apertures.

4. SED FITTING

4.1. Redshift estimation

Based on the UV to MIR photometric catalog, we first estimate the photometric redshifts by running SED fitting with EAZY (G. B. Brammer et al. 2008). Before SED fitting, the galactic extinctions of all flux measurements are corrected using the dust map from E. F. Schlafly & D. P. Finkbeiner (2011). For flux densities with $\text{SNR} < 2$, we consider them to be unreliable and only use their value of $3 \times f_{\text{err}}$ as the upper limits. For the other flux densities from high-resolution data and low-resolution data, we apply 5% and 10% systematic error floors, respectively. Then, we adopt

the `_blue_sfhz_13` template library, which contains models dominated by strong emission lines, to obtain the minimum χ^2 redshifts with EAZY in the extended redshift range $z = 0 - 16$.

In addition to the photometric redshifts, we collect the available spectroscopic redshifts for our catalog. We first collect all publicly available JWST spectroscopy in the PRIMER-COSMOS and UDS fields from the DAWN JWST Archive (DJA v3.0). These JWST spectra have been reduced with the *MSAEXP* pipeline (G. Brammer 2023) following the methods described in A. de Graaff et al. (2025) and K. E. Heintz et al. (2024). For the galaxies without JWST spectroscopy, we further search for the spectroscopic redshifts measured by other telescopes. In PRIMER-COSMOS, A. A. Khostovan et al. (2025) collects the spectroscopic redshifts from 108 different programs observed in the last 20 years. In PRIMER-UDS, we use the spectroscopic redshifts collected by the FENIKS catalog (K. Zaidi et al. 2024) and the VLT/VIMOS spectroscopy from the VANDELS survey (M. Talia et al. 2023). Combining those surveys, 10551 galaxies are found to have spectroscopic redshifts with high confidence levels, including 5379 in COSMOS and 5172 in UDS.

4.2. Physical properties from Bagpipes

Once the redshifts of galaxies are determined, we then perform SED fitting with fixed redshifts using Bagpipes (A. C. Carnall et al. 2018) to estimate their physical properties, including but not limited to the stellar masses, star formation rates, and the rest-frame col-

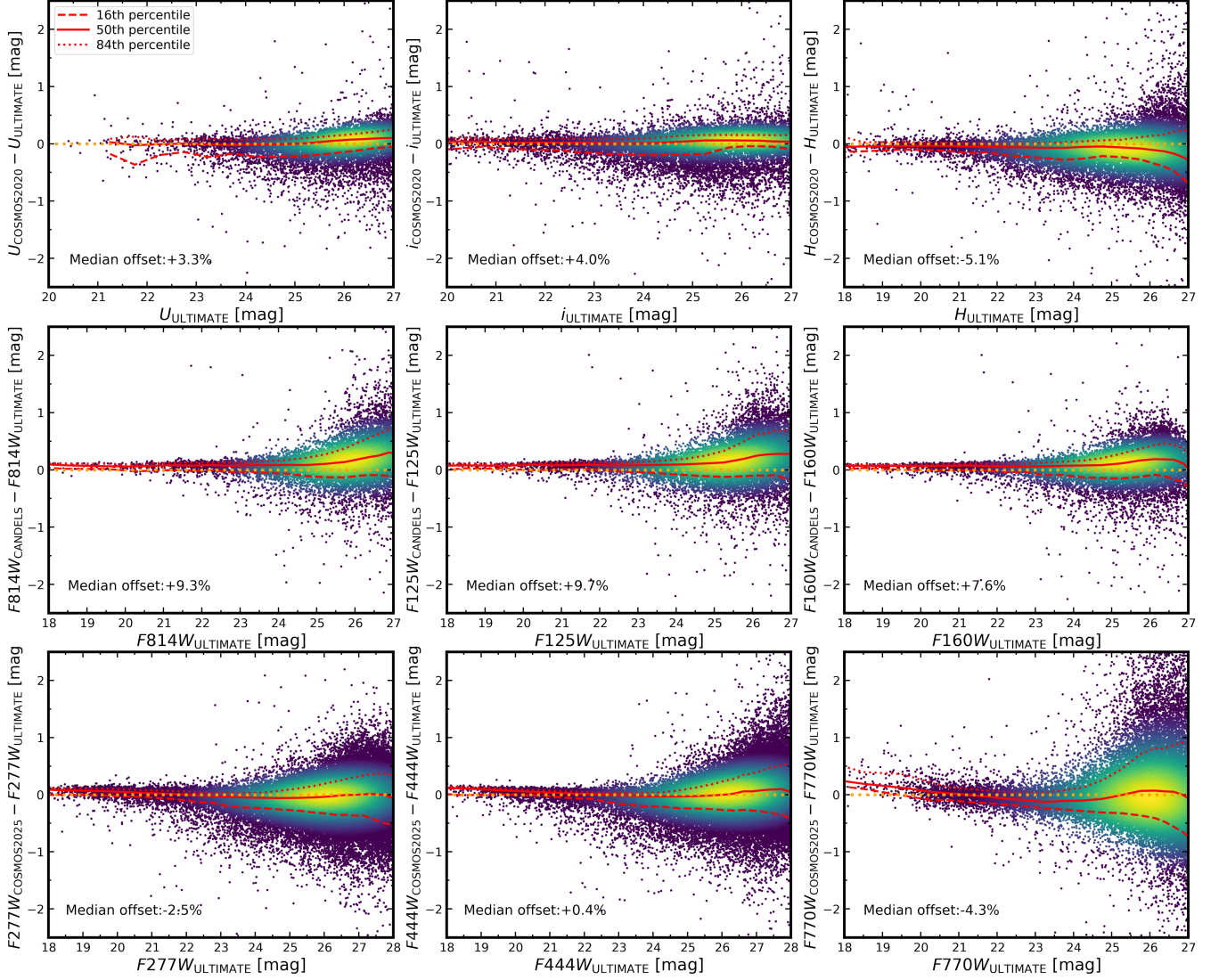


Figure 8. Comparison between our catalog and archival results in PRIMER-COSMOS. The upper panels compare the flux densities observed by ground-based telescopes from our ULTIMATE-deblending catalog and the COSMOS2020 catalog (J. R. Weaver et al. 2022). The middle panels compare the HST fluxes from our catalog and the CANDELS catalog (H. Nayyeri et al. 2017). The CANDELS catalog directly uses the flux densities measured by Kron apertures as total flux densities, which can underestimate the total fluxes of faint sources with small Kron apertures. The lower panels compare the JWST flux densities measured by our catalog and the COSMOS2025 catalog (M. Shuntov et al. 2025). The median offsets are reported for all sources with $\text{SNR} > 7$ in each corresponding band.

ors. For Bagpipes, we adopt the 2016 revision of the G. Bruzual & S. Charlot (2003) stellar-population synthesis models. Stellar ages are allowed to vary between 0.03-10 Gyr while metallicities span $Z/Z_{\odot} = 0.01 - 2.5$. The star-formation history is parameterized as a delayed exponential with a timescale $\tau \in [0.01, 10]$ Gyr. Dust attenuation is modeled with the D. Calzetti et al. (2000) model, which is allowed to be $A_V \in [0, 5]$ and has been applied separately to young ($< 0.01\text{Gyr}$) and old ($> 0.01\text{Gyr}$) stellar populations. Nebular emission is added following the N. Byler et al. (2017) pre-

scription with the ionization parameter constrained to $\log U \in [-5, -2]$.

Figure 9 presents the distribution of the redshifts and galaxy stellar masses in our catalog. To estimate the stellar mass completeness limit of our catalog, we adopt the method described by L. Pozzetti et al. (2010), which is also used by many other catalogs (e.g. C. Laigle et al. 2016; J. R. Weaver et al. 2022; M. Shuntov et al. 2025). In brief, for each source, we calculate its limiting stellar mass at which it can be detected at the magnitude limit

$$\log M_{*,\text{lim}} = \log M_* - 0.4(\text{mag}_{F444W,\text{lim}} - \text{mag}_{F444W}), \quad (4)$$

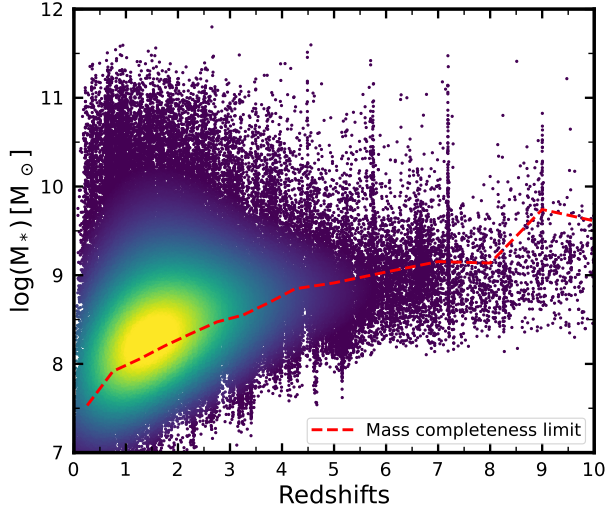


Figure 9. Distribution of the redshifts and galaxy stellar masses in our catalog. The red dashed line shows the stellar mass completeness limit as a function of redshift, which is calculated following [L. Pozzetti et al. \(2010\)](#). Our catalog can provide a mass-complete sample of galaxies at $\log(M_*/M_\odot) > 9$ up to $z \sim 8.5$.

where $\text{mag}_{F444W, \text{lim}} = 27.2$ is the limiting magnitude of our catalog (see Section 3.2). Then, we take the 90th percentile of $\log M_{*, \text{lim}}$ in each redshift bin as the limiting stellar mass. Based on this estimation, our catalog can provide an unbiased mass-complete census of high-redshift galaxies up to $z \sim 8.5$, while the sample at $z > 9$ might be biased to the brightest galaxies. We note that the density peak at $z \sim 7.15$ is because many strong [OIII] emitters at $z = 6.8 - 7.5$ with flux excess in the F410M medium band are fitted at $z \sim 7.15$ by Eazy, which should be considered during the determination of redshift bins. We also remind that for the area without JWST/MIRI coverage, the stellar masses of massive galaxies at $z > 5.5$ might be over-estimated as shown in [T. Wang et al. \(2025\)](#).

5. DISCUSSION: IMPROVED PHOTOMETRIC REDSHIFTS WITH LOW-RESOLUTION DATA

Compared with the previous JWST-based catalogs, a key improvement of our work is to make use of the abundant archival low-resolution data in the PRIMER-COSMOS and UDS fields. These low-resolution data help to improve the quality of SED fitting in two ways: Firstly, the deep images from CFHT and Subaru provide better constraints on the SED in the UV-to-optical bands, which greatly help to break the degeneracy during SED fitting. Figure 10 shows an example of this issue: Using the HST and JWST data, the galaxy COSMOS-18376 is fitted at $z_{\text{phot}} = 0.80$ with a Balmer break at $\lambda_{\text{obs}} \sim 0.7 \mu\text{m}$. Once the low-resolution data

are considered, it is clear that this Balmer break is actually a Lyman break. Therefore, its photometric redshift is corrected to be $z_{\text{phot}} = 4.78$, which is close to the spectroscopic redshift $z_{\text{spec}} = 4.82$. On the other hand, Subaru, VISTA, and Magellan can provide additional medium- and narrow-band data, which helps identify SED features such as emission lines and breaks. For example, the medium band H_1 from the ZFOURGE survey ([C. M. S. Straatman et al. 2016](#)) identified the [O III] emission line for the galaxy UDS-22688 at $z_{\text{spec}} = 2.50$, which was previously considered to be a low-redshift galaxy with only the high-resolution data.

In Figure 11, we test the reliability of our photometric redshifts by comparing them to the spectroscopic redshifts. Firstly, when we only use the high-resolution data (from HST, JWST/NIRCam and MIRI) without ground-based data (w/o GD), the photometric redshifts are found to have a scatter $\sigma_{\text{NMAD}} = 0.027$ and outlier fraction $f_{\text{outlier}}(|z_{\text{spec}} - z_{\text{phot}}| / (z_{\text{spec}} + 1) > 0.15) = 5.3\%$. Similar to [E. Merlin et al. \(2024\)](#), the unreliable sources identified by the flags in our catalog and the AGN candidates (e.g., the Little Red Dots selected by [T. Wang et al. 2025](#)) are excluded from this comparison. We found that our result without low-resolution data is comparable to the ASTRODEEP-JWST catalog from [E. Merlin et al. \(2024\)](#), who reported $\sigma_{\text{NMAD}} = 0.033$ (0.033) and $f_{\text{outlier}} = 6.1\%$ (4.5%) in PRIMER-COSMOS (UDS). Once we add the low-resolution data, the quality of photometric redshifts can be improved with $\sigma_{\text{NMAD}} = 0.016$ and $f_{\text{outlier}} = 2.2\%$. If we only focus on the subsample of galaxies with $|z_{\text{phot}, \text{w GD}} - z_{\text{phot}, \text{w/o GD}}| > 0.5$, the outlier fraction in the JWST+HST catalog reaches $f_{\text{outlier}} = 88\%$, while the outlier fraction in the full UV to MIR catalog is only $f_{\text{outlier}} = 12\%$.

In PRIMER-COSMOS, the photometric redshifts reported by our catalog have $\sigma_{\text{NMAD}} = 0.013$ and $f_{\text{outlier}} = 1.7\%$. After cross-matching this same spectroscopic sample with the COSMOS2025 catalog ([M. Shuntov et al. 2025](#)), we found that the photometric redshifts from COSMOS2025 have $\sigma_{\text{NMAD}} = 0.016$ and $f_{\text{outlier}} = 5.3\%$. Since COSMOS2025 has also combined the JWST data with the low-resolution ground-based data, our key improvement compared to COSMOS2025 is that the JWST mosaics used by our work are much deeper and have more bands.

In the lower right panel of Figure 11, we remove the requirement for spectroscopic data and check the fraction of galaxies with $|z_{\text{phot}, \text{w GD}} - z_{\text{phot}, \text{w/o GD}}| > 0.5$ in the entire catalog. After excluding the area with only the shallow JWST/NIRCam (F140M, F430M, and F460M) observations from the BEACON survey ([T. Morishita](#)

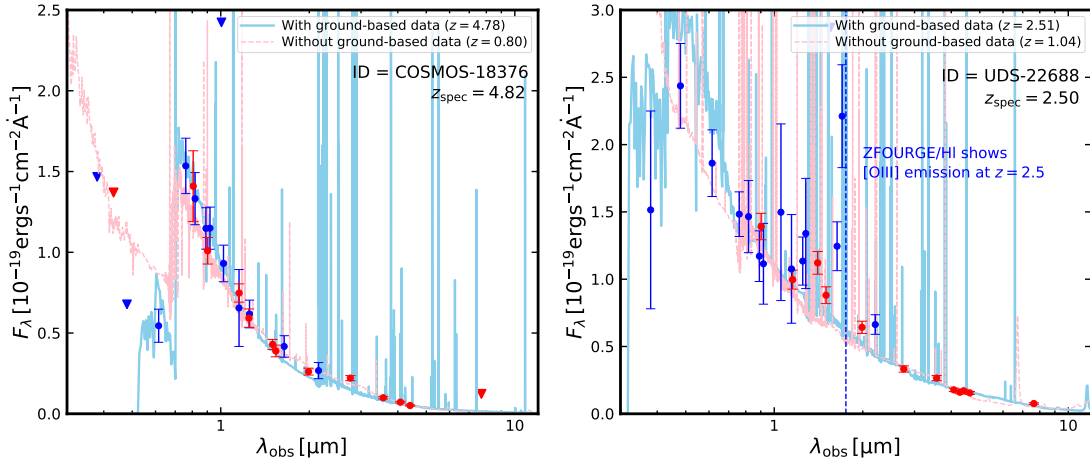


Figure 10. Examples of galaxies with improved photometric redshifts with low-resolution data The red and blue points show the photometric results from high-resolution and low-resolution data, respectively. The red lines show the best-fit SED from EAZY when we only use the high-resolution data from HST and JWST. The blue lines show the best-fit SED based on the full multi-wavelength catalog, including the low-resolution ground-based data.

et al. 2025) and the faint sources with $\text{SNR}_{F444W} < 7$, we found that $\sim 25 - 30\%$ of the massive galaxies at $z \gtrsim 4$ could have incorrect photometric redshifts without the low-resolution data. Many of these galaxies are similar to COSMOS-18376 in Figure 10, with their Lyman breaks mistaken as Balmer breaks at lower redshifts. Using the redshifts and stellar masses based on our catalog, the galaxy build-up is smoother across a large redshift range (T. Wang et al. 2025) compared with previous results reporting rapid build-up of massive galaxies at $z = 4 - 6$ based on catalogs without low-resolution data (A. Weibel et al. 2024). We remind that the quantitative results shown in Figure 11 are dependent on the quality of the multi-wavelength data collection. As shown by the dashed lines, the ratio of massive galaxies with different photometric redshifts can be reduced from $\sim 25 - 30\%$ to $\sim 15\%$ when the high-resolution optical HST data are available from the CANDELS survey. This suggests that although the optical data from HST helps to improve the photometric redshifts, the low-resolution ground-based data are still required to give the best estimations of photometric redshifts.

6. CONCLUSIONS

In this paper, we presented the first data release of the ULTIMATE-deblending project: the deblended photometric catalog across UV to MIR based on JWST/PRIMER. We present the reduction of JWST mosaics, the construction of the UV to MIR photometric catalog, and the SED fitting. The JWST mosaics and catalogs listing the results of multi-wavelength photometry and SED fitting will be publicly released on (106.14.163.220/ultimate/) once this paper is accepted.

Based on the deep JWST images in the PRIMER-COSMOS and PRIMER-UDS fields reduced by our modified JWST pipeline, we performed dual-mode source extraction on the combined NIRCcam LW image. We conducted aperture photometry with PSF matching for the high-resolution data from JWST/NIRCcam and HST, and TPHOT deblending photometry for the other bands with lower resolutions. This yields a 50-band UV-to-MIR catalog for 308239 sources in a survey area of 627.1 arcmin².

Using this comprehensive multi-wavelength catalog, we performed SED fitting to obtain the photometric redshifts and physical properties of the detected sources. We discussed that the additional bands from low-resolution ground-based telescopes improve the accuracy of photometric redshifts by providing extended wavelength coverage in the UV to optical and emphasizing the emission lines and breaks. These accurate photometric redshifts are the foundation of a reliable photometric census of high-redshift galaxies.

In the following works of the ULTIMATE-deblending project, we will further collect new JWST observations in the PRIMER fields, extend our project to the FIR and Radio bands, and then construct UV to Radio catalogs for other JWST deep fields. These will provide a high-quality reference sample of high-redshift galaxies, enabling robust constraints on the stellar mass assembly history of galaxies in the early universe.

ACKNOWLEDGEMENTS

We thank Dr. Mark Dickinson and Dr. James Dunlop for the helpful comments on this paper. This work was supported by National Natural Science Found-

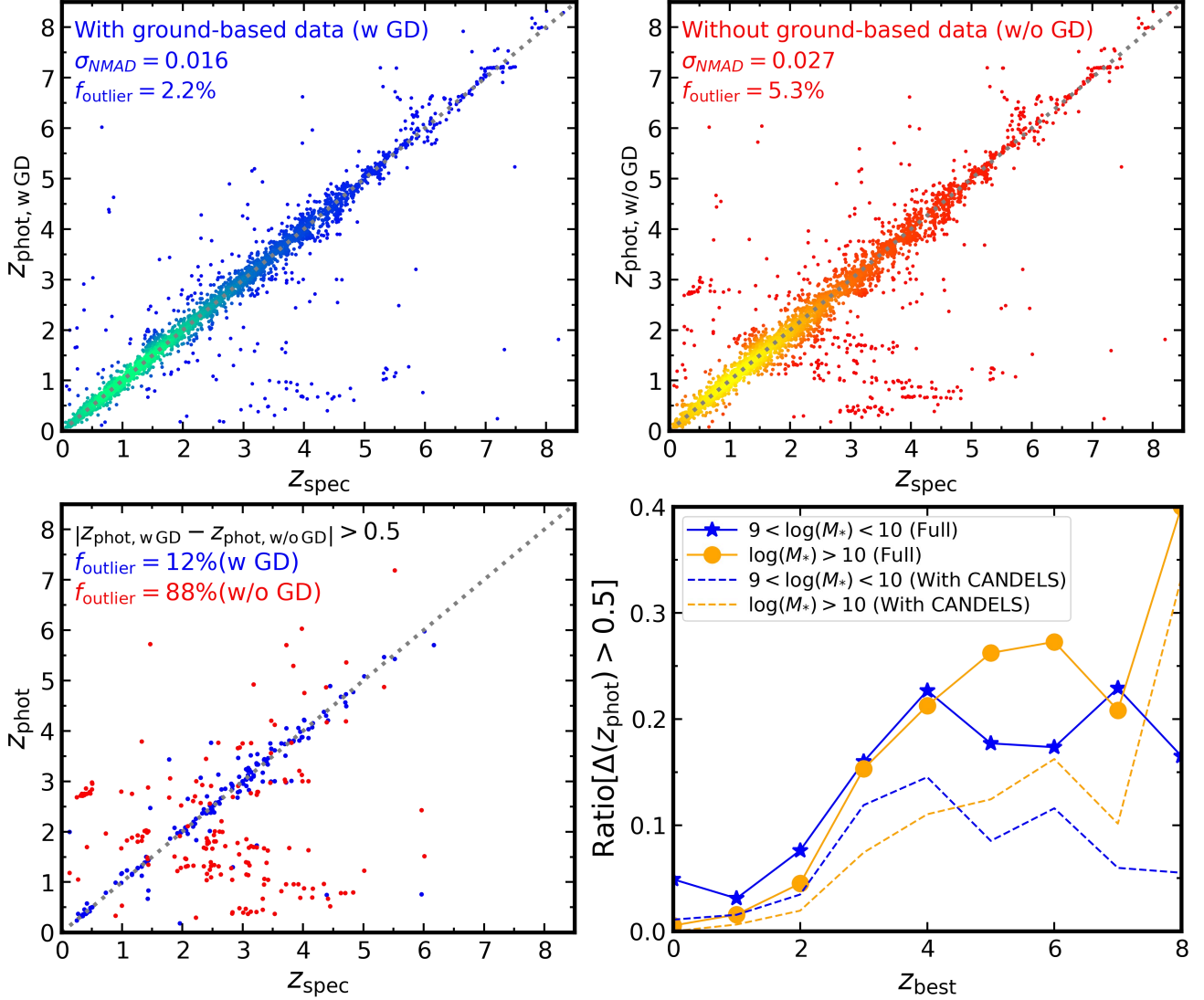


Figure 11. Validation of photometric redshifts. **Upper left:** The comparison between photometric redshifts and spectroscopic redshifts in our final catalog with ground-based data. **Upper right** The same comparison when we only use the high-resolution data from HST and JWST. **Lower left:** The photometric and spectroscopic redshift comparison for galaxies that have different photometric redshifts ($|z_{\text{phot, wGD}} - z_{\text{phot, w/oGD}}| > 0.5$), the blue and red points represent the results with and without ground-based data, respectively. **Lower right:** The ratio of galaxies with different photometric redshifts ($|z_{\text{phot, wGD}} - z_{\text{phot, w/oGD}}| > 0.5$) as a function of redshift. The blue line and orange line shows the ratio of small galaxies ($9 < \log(M_*/M_\odot) < 10$) and massive galaxies ($\log(M_*/M_\odot) > 10$), respectively. The solid and dashed lines show the ratios in the entire catalog and the region covered by the high-resolution HST data from the CANDELS survey, respectively.

dation of China (Grant No.12525302 and 12141301), Natural Science Foundation of Jiangsu Higher Education Institutions of China(Grant No. BK20250001), National Key R&D Program of China (Grant no. 2023YFA1605600), Scientific Research Innovation Capability Support Project for Young Faculty (Project No. ZYGXQNJSKYCXNLZCXM-P3), the Fundamental Research Funds for the Central Universities with Grant no.KG202502, and the China Manned Space Program with grant no. CMS-CSST-2025-A04. JSD acknowledges the support of the Royal Society through

the award of a Royal Society Research Professorship. Y.J.W. acknowledges supports by Jiangsu Natural Science Foundation (Project No. BK20241188) and National Natural Science Foundation of China (Project No. 12403019). V.Sangalli acknowledge the support of France 2030 through the project named Académie Spatiale d’Île-de-France (<https://academiespatiale.fr/>) managed by the National Research Agency under bearing the reference ANR-23-CMAS-0041.

This work is based on observations made with the NASA/ESA/CSA James Webb Space Telescope. The

raw JWST imaging data are obtained from the Mikulski Archive for Space Telescopes (MAST) and are available at [10.17909/e1wh-b970](https://archive.stsci.edu/missions/jwst). MAST is operated by the Association of Universities for Research in Astronomy, Inc., under NASA contract NAS 5–03127 for JWST. These observations are associated with programmes 1727, 1837, 1840, 2321, 2514, and 3990.

The HST mosaics and the JWST spectroscopic data used in this work are collected from the Dawn JWST Archive (DJA). DJA is an initiative of the Cosmic Dawn Center (DAWN), which is funded by the Danish National Research Foundation under grant DNR140.

The images of VISTA/VIRCAM are based on observations collected at the European Southern Observatory under ESO programmes 179.A-2005 and 198.A-2003, data obtained from the ESO Science Archive Facility with DOI <https://doi.org/10.18727/archive/52>, and data products produced by CALET and the Cambridge Astronomy Survey Unit on behalf of the UltraVISTA consortium.

UKIDSS was undertaken on UKIRT while it was operated by the Joint Astronomy Centre on behalf of the Science and Technology Facilities Council of the UK, which also provided support for the Cambridge Astronomical Survey Unit (CASU) and the Edinburgh Wide Field Astronomy Unit (WFAU) that generated and served the wide-field infrared public surveys from UKIRT.

The images of Subaru/HSC are provided by the Hyper Suprime-Cam (HSC) collaboration, which includes the astronomical communities of Japan and Taiwan, and Princeton University. The HSC instrumentation and software were developed by the National Astronomical Observatory of Japan (NAOJ), the Kavli Institute for the Physics and Mathematics of the Universe (Kavli IPMU), the University of Tokyo, the High Energy Accelerator Research Organization (KEK), the Academia Sinica Institute for Astronomy and Astrophysics in Taiwan (ASIAA), and Princeton University. Funding was contributed by the FIRST program from the Japanese Cabinet Office, the Ministry of Education, Culture, Sports, Science and Technology (MEXT), the Japan Society for the Promotion of Science (JSPS), Japan Science and Technology Agency (JST), the Toray Science Foundation, NAOJ, Kavli IPMU, KEK, ASIAA, and Princeton University. These Subaru/HSC data make use of software developed for the Vera C. Rubin Observatory. We thank the Rubin Observatory for making their code available as free software at <http://pipelines.lsst.io/>. The Subaru/HSC data were collected at the Subaru Telescope and retrieved from the HSC data archive system, which is operated by the Subaru Telescope and Astronomy Data Center (ADC) at NAOJ. Data analysis was in part carried out with the cooperation of Center for Computational Astrophysics (CfCA), NAOJ. We are honored and grateful for the opportunity of observing the Universe from Maunakea, which has the cultural, historical and natural significance in Hawaii.

REFERENCES

- Aihara, H., AlSayyad, Y., Ando, M., et al. 2022, *PASJ*, 74, 247, doi: [10.1093/pasj/psab122](https://doi.org/10.1093/pasj/psab122)
- Alvarez-Marquez, J., Hashimoto, T., Arribas, S., et al. 2021, ALMA [OIII]88um Emitters. Signpost of Early Stellar Buildup and Reionization in the Universe., JWST Proposal. Cycle 1, ID. #1840
- Astropy Collaboration, Price-Whelan, A. M., Lim, P. L., et al. 2022, *ApJ*, 935, 167, doi: [10.3847/1538-4357/ac7c74](https://doi.org/10.3847/1538-4357/ac7c74)
- Bagley, M. B., Finkelstein, S. L., Koekemoer, A. M., et al. 2023, *ApJL*, 946, L12, doi: [10.3847/2041-8213/acbb08](https://doi.org/10.3847/2041-8213/acbb08)
- Bertin, E., & Arnouts, S. 1996, *A&AS*, 117, 393, doi: [10.1051/aas:1996164](https://doi.org/10.1051/aas:1996164)
- Bezanson, R., Labbe, I., Whitaker, K. E., et al. 2024, *ApJ*, 974, 92, doi: [10.3847/1538-4357/ad66cf](https://doi.org/10.3847/1538-4357/ad66cf)
- Bradley, L., Sipőcz, B., Robitaille, T., et al. 2022, *astropy/photutils*: 1.5.0, 1.5.0 Zenodo, doi: [10.5281/zenodo.6825092](https://doi.org/10.5281/zenodo.6825092)
- Brammer, G. 2023, *msaexp*: NIRSpec analysis tools, 0.6.17 Zenodo, doi: [10.5281/zenodo.7299500](https://doi.org/10.5281/zenodo.7299500)
- Brammer, G. B., van Dokkum, P. G., & Coppi, P. 2008, *ApJ*, 686, 1503, doi: [10.1086/591786](https://doi.org/10.1086/591786)
- Bruzual, G., & Charlot, S. 2003, *MNRAS*, 344, 1000, doi: [10.1046/j.1365-8711.2003.06897.x](https://doi.org/10.1046/j.1365-8711.2003.06897.x)
- Bushouse, H., Eisenhamer, J., Dencheva, N., et al. 2024, JWST Calibration Pipeline, 1.13.4 Zenodo, doi: [10.5281/zenodo.10569856](https://doi.org/10.5281/zenodo.10569856)
- Bushouse, H., Eisenhamer, J., Dencheva, N., et al. 2025, JWST Calibration Pipeline, 1.19.1 Zenodo, doi: [10.5281/zenodo.16280965](https://doi.org/10.5281/zenodo.16280965)
- Byler, N., Dalcanton, J. J., Conroy, C., & Johnson, B. D. 2017, *ApJ*, 840, 44, doi: [10.3847/1538-4357/aa6c66](https://doi.org/10.3847/1538-4357/aa6c66)
- Calzetti, D., Armus, L., Bohlin, R. C., et al. 2000, *ApJ*, 533, 682, doi: [10.1086/308692](https://doi.org/10.1086/308692)
- Carnall, A. C., McLure, R. J., Dunlop, J. S., & Davé, R. 2018, *MNRAS*, 480, 4379, doi: [10.1093/mnras/sty2169](https://doi.org/10.1093/mnras/sty2169)

- Casey, C. M., Kartaltepe, J. S., Drakos, N. E., et al. 2023, *ApJ*, 954, 31, doi: [10.3847/1538-4357/acc2bc](https://doi.org/10.3847/1538-4357/acc2bc)
- de Graaff, A., Brammer, G., Weibel, A., et al. 2025, *A&A*, 697, A189, doi: [10.1051/0004-6361/202452186](https://doi.org/10.1051/0004-6361/202452186)
- Di Criscienzo, M., Merlin, E., Castellano, M., et al. 2017, *A&A*, 607, A30, doi: [10.1051/0004-6361/201731172](https://doi.org/10.1051/0004-6361/201731172)
- Duncan, K. J., McLeod, D. J., Best, P. N., et al. 2025, *MNRAS*, 541, 1329, doi: [10.1093/mnras/staf1061](https://doi.org/10.1093/mnras/staf1061)
- Dunlop, J. S., Abraham, R. G., Ashby, M. L. N., et al. 2021, PRIMER: Public Release IMaging for Extragalactic Research., JWST Proposal. Cycle 1, ID. #1837
- Eisenstein, D. J., Willott, C., Alberts, S., et al. 2026, *ApJS*, 283, 6, doi: [10.3847/1538-4365/ae3163](https://doi.org/10.3847/1538-4365/ae3163)
- Euclid Collaboration, Mellier, Y., Abdurro'uf, et al. 2025, *A&A*, 697, A1, doi: [10.1051/0004-6361/202450810](https://doi.org/10.1051/0004-6361/202450810)
- Finkelstein, S. L., Bagley, M. B., Ferguson, H. C., et al. 2023, *ApJL*, 946, L13, doi: [10.3847/2041-8213/acad4](https://doi.org/10.3847/2041-8213/acad4)
- Franco, M., Elbaz, D., Béthermin, M., et al. 2018, *A&A*, 620, A152, doi: [10.1051/0004-6361/201832928](https://doi.org/10.1051/0004-6361/201832928)
- Gaia Collaboration, Brown, A. G. A., Vallenari, A., et al. 2018, *A&A*, 616, A1, doi: [10.1051/0004-6361/201833051](https://doi.org/10.1051/0004-6361/201833051)
- Galametz, A., Grazian, A., Fontana, A., et al. 2013, *ApJS*, 206, 10, doi: [10.1088/0067-0049/206/2/10](https://doi.org/10.1088/0067-0049/206/2/10)
- Gao, Z.-K., Lim, C.-F., Wang, W.-H., et al. 2024, *ApJ*, 971, 117, doi: [10.3847/1538-4357/ad53c1](https://doi.org/10.3847/1538-4357/ad53c1)
- Guo, Y., Ferguson, H. C., Giavalisco, M., et al. 2013, *ApJS*, 207, 24, doi: [10.1088/0067-0049/207/2/24](https://doi.org/10.1088/0067-0049/207/2/24)
- Hale, C. L., Heywood, I., Jarvis, M. J., et al. 2025, *MNRAS*, 536, 2187, doi: [10.1093/mnras/stae2528](https://doi.org/10.1093/mnras/stae2528)
- Heintz, K. E., Watson, D., Brammer, G., et al. 2024, *Science*, 384, 890, doi: [10.1126/science.adj0343](https://doi.org/10.1126/science.adj0343)
- Huang, J.-S., Zheng, X. Z., Rigopoulou, D., et al. 2011, *ApJL*, 742, L13, doi: [10.1088/2041-8205/742/1/L13](https://doi.org/10.1088/2041-8205/742/1/L13)
- Ji, Z., Williams, C. C., Tacchella, S., et al. 2024, *ApJ*, 974, 135, doi: [10.3847/1538-4357/ad6e7f](https://doi.org/10.3847/1538-4357/ad6e7f)
- Jin, S., Daddi, E., Liu, D., et al. 2018, *ApJ*, 864, 56, doi: [10.3847/1538-4357/aad4af](https://doi.org/10.3847/1538-4357/aad4af)
- Kartaltepe, J. S., Rose, C., Vanderhoof, B. N., et al. 2023, *ApJL*, 946, L15, doi: [10.3847/2041-8213/acad01](https://doi.org/10.3847/2041-8213/acad01)
- Khostovan, A. A., Kartaltepe, J. S., Salvato, M., et al. 2025, arXiv e-prints, arXiv:2503.00120, doi: [10.48550/arXiv.2503.00120](https://doi.org/10.48550/arXiv.2503.00120)
- Kocevski, D. D., Finkelstein, S. L., Barro, G., et al. 2025, *ApJ*, 986, 126, doi: [10.3847/1538-4357/adbc7d](https://doi.org/10.3847/1538-4357/adbc7d)
- Koekemoer, A. M., Avila, R. J., Hammer, D., et al. 2014, in American Astronomical Society Meeting Abstracts, Vol. 223, American Astronomical Society Meeting Abstracts #223, 254.02
- Kron, R. G. 1980, *ApJS*, 43, 305, doi: [10.1086/190669](https://doi.org/10.1086/190669)
- Kroupa, P. 2001, *MNRAS*, 322, 231, doi: [10.1046/j.1365-8711.2001.04022.x](https://doi.org/10.1046/j.1365-8711.2001.04022.x)
- Labbe, I., Greene, J. E., Bezanson, R., et al. 2025, *ApJ*, 978, 92, doi: [10.3847/1538-4357/ad3551](https://doi.org/10.3847/1538-4357/ad3551)
- Laigle, C., McCracken, H. J., Ilbert, O., et al. 2016, *ApJS*, 224, 24, doi: [10.3847/0067-0049/224/2/24](https://doi.org/10.3847/0067-0049/224/2/24)
- Liu, D., Daddi, E., Dickinson, M., et al. 2018, *ApJ*, 853, 172, doi: [10.3847/1538-4357/aaa600](https://doi.org/10.3847/1538-4357/aaa600)
- Liu, W., & Jiang, L. 2026, arXiv e-prints, arXiv:2602.04179, doi: [10.48550/arXiv.2602.04179](https://doi.org/10.48550/arXiv.2602.04179)
- Lotz, J., Mountain, M., Grogin, N. A., et al. 2014, in American Astronomical Society Meeting Abstracts, Vol. 223, American Astronomical Society Meeting Abstracts #223, 254.01
- Masters, D., Capak, P., Stern, D., et al. 2015, *ApJ*, 813, 53, doi: [10.1088/0004-637X/813/1/53](https://doi.org/10.1088/0004-637X/813/1/53)
- McCracken, H. J., Milvang-Jensen, B., Dunlop, J., et al. 2012, *A&A*, 544, A156, doi: [10.1051/0004-6361/201219507](https://doi.org/10.1051/0004-6361/201219507)
- Mehta, V., Scarlata, C., Capak, P., et al. 2018, *ApJS*, 235, 36, doi: [10.3847/1538-4365/aab60c](https://doi.org/10.3847/1538-4365/aab60c)
- Mehta, V., Rafelski, M., Sunnquist, B., et al. 2024, *ApJS*, 275, 17, doi: [10.3847/1538-4365/ad7d8f](https://doi.org/10.3847/1538-4365/ad7d8f)
- Merlin, E., Pilo, S., Fontana, A., et al. 2019, *A&A*, 622, A169, doi: [10.1051/0004-6361/201833991](https://doi.org/10.1051/0004-6361/201833991)
- Merlin, E., Fontana, A., Ferguson, H. C., et al. 2015, *A&A*, 582, A15, doi: [10.1051/0004-6361/201526471](https://doi.org/10.1051/0004-6361/201526471)
- Merlin, E., Bourne, N., Castellano, M., et al. 2016a, *A&A*, 595, A97, doi: [10.1051/0004-6361/201628751](https://doi.org/10.1051/0004-6361/201628751)
- Merlin, E., Amorín, R., Castellano, M., et al. 2016b, *A&A*, 590, A30, doi: [10.1051/0004-6361/201527513](https://doi.org/10.1051/0004-6361/201527513)
- Merlin, E., Castellano, M., Santini, P., et al. 2021, *A&A*, 649, A22, doi: [10.1051/0004-6361/202140310](https://doi.org/10.1051/0004-6361/202140310)
- Merlin, E., Santini, P., Paris, D., et al. 2024, *A&A*, 691, A240, doi: [10.1051/0004-6361/202451409](https://doi.org/10.1051/0004-6361/202451409)
- Morishita, T., Mason, C. A., Kreilgaard, K. C., et al. 2025, *ApJ*, 983, 152, doi: [10.3847/1538-4357/adbbdc](https://doi.org/10.3847/1538-4357/adbbdc)
- Nayyeri, H., Hemmati, S., Mobasher, B., et al. 2017, *ApJS*, 228, 7, doi: [10.3847/1538-4365/228/1/7](https://doi.org/10.3847/1538-4365/228/1/7)
- Oke, J. B., & Gunn, J. E. 1983, *ApJ*, 266, 713, doi: [10.1086/160817](https://doi.org/10.1086/160817)
- Osborne, S., Perrin, M. D., & Melendez Hernandez, M. 2018, in American Astronomical Society Meeting Abstracts, Vol. 232, American Astronomical Society Meeting Abstracts #232, 119.12
- Papovich, C., Cole, J. W., Yang, G., et al. 2023, *ApJL*, 949, L18, doi: [10.3847/2041-8213/acc948](https://doi.org/10.3847/2041-8213/acc948)
- Pérez-González, P. G., Barro, G., Rieke, G. H., et al. 2024, *ApJ*, 968, 4, doi: [10.3847/1538-4357/ad38bb](https://doi.org/10.3847/1538-4357/ad38bb)

- Perrin, M. D., Long, J., Sivaramakrishnan, A., et al. 2015, WebbPSF: James Webb Space Telescope PSF Simulation Tool., Astrophysics Source Code Library, record ascl:1504.007
- Pozzetti, L., Bolzonella, M., Zucca, E., et al. 2010, *A&A*, 523, A13, doi: [10.1051/0004-6361/200913020](https://doi.org/10.1051/0004-6361/200913020)
- Rieke, M. J., Robertson, B., Tacchella, S., et al. 2023, *ApJS*, 269, 16, doi: [10.3847/1538-4365/acf44d](https://doi.org/10.3847/1538-4365/acf44d)
- Roster, W., Wright, A. H., Hildebrandt, H., et al. 2025, arXiv e-prints, arXiv:2508.02779, doi: [10.48550/arXiv.2508.02779](https://doi.org/10.48550/arXiv.2508.02779)
- Sanders, D. B., Salvato, M., Aussel, H., et al. 2007, *ApJS*, 172, 86, doi: [10.1086/517885](https://doi.org/10.1086/517885)
- Schlafly, E. F., & Finkbeiner, D. P. 2011, *ApJ*, 737, 103, doi: [10.1088/0004-637X/737/2/103](https://doi.org/10.1088/0004-637X/737/2/103)
- Scoville, N., Aussel, H., Brusa, M., et al. 2007, *ApJS*, 172, 1, doi: [10.1086/516585](https://doi.org/10.1086/516585)
- Shuntov, M., Akins, H. B., Paquereau, L., et al. 2025, *A&A*, 704, A339, doi: [10.1051/0004-6361/202555799](https://doi.org/10.1051/0004-6361/202555799)
- Skelton, R. E., Whitaker, K. E., Momcheva, I. G., et al. 2014, *ApJS*, 214, 24, doi: [10.1088/0067-0049/214/2/24](https://doi.org/10.1088/0067-0049/214/2/24)
- Smolčić, V., Novak, M., Bondi, M., et al. 2017, *A&A*, 602, A1, doi: [10.1051/0004-6361/201628704](https://doi.org/10.1051/0004-6361/201628704)
- Song, J., Fang, G., Lin, Z., Gu, Y., & Kong, X. 2023, *ApJ*, 958, 82, doi: [10.3847/1538-4357/ad0365](https://doi.org/10.3847/1538-4357/ad0365)
- SpUDS Team. 2020, Spitzer Public Legacy Survey of the UKIDSS Ultra Deep Survey., NASA IPAC DataSet, IRSA403 doi: [10.26131/IRSA403](https://doi.org/10.26131/IRSA403)
- Steinhardt, C. L., Speagle, J. S., Capak, P., et al. 2014, *ApJL*, 791, L25, doi: [10.1088/2041-8205/791/2/L25](https://doi.org/10.1088/2041-8205/791/2/L25)
- Straatman, C. M. S., Spitler, L. R., Quadri, R. F., et al. 2016, *ApJ*, 830, 51, doi: [10.3847/0004-637X/830/1/51](https://doi.org/10.3847/0004-637X/830/1/51)
- Sun, F., Yang, J., Wang, F., et al. 2025, arXiv e-prints, arXiv:2506.06418, doi: [10.48550/arXiv.2506.06418](https://doi.org/10.48550/arXiv.2506.06418)
- Sun, H., Wang, T., Xu, K., et al. 2024, *ApJL*, 967, L34, doi: [10.3847/2041-8213/ad4986](https://doi.org/10.3847/2041-8213/ad4986)
- Sun, H., Wang, T., Daddi, E., et al. 2025, *ApJL*, 993, L49, doi: [10.3847/2041-8213/ae1132](https://doi.org/10.3847/2041-8213/ae1132)
- Talia, M., Schreiber, C., Garilli, B., et al. 2023, *A&A*, 678, A25, doi: [10.1051/0004-6361/202346293](https://doi.org/10.1051/0004-6361/202346293)
- Wang, B., Leja, J., Atek, H., et al. 2024, *ApJ*, 963, 74, doi: [10.3847/1538-4357/ad187c](https://doi.org/10.3847/1538-4357/ad187c)
- Wang, T., Schreiber, C., Elbaz, D., et al. 2019, *Nature*, 572, 211, doi: [10.1038/s41586-019-1452-4](https://doi.org/10.1038/s41586-019-1452-4)
- Wang, T., Sun, H., Zhou, L., et al. 2025, *ApJL*, 988, L35, doi: [10.3847/2041-8213/adebe7](https://doi.org/10.3847/2041-8213/adebe7)
- Wang, W.-H., Lin, W.-C., Lim, C.-F., et al. 2017, *ApJ*, 850, 37, doi: [10.3847/1538-4357/aa911b](https://doi.org/10.3847/1538-4357/aa911b)
- Wang, W.-H., Foucaud, S., Hsieh, B.-C., et al. 2022, *ApJS*, 260, 54, doi: [10.3847/1538-4365/ac729e](https://doi.org/10.3847/1538-4365/ac729e)
- Wang, Z., Wang, T., Xu, K., et al. 2025, arXiv e-prints, arXiv:2510.00187, doi: [10.48550/arXiv.2510.00187](https://doi.org/10.48550/arXiv.2510.00187)
- Weaver, J. R., Kauffmann, O. B., Ilbert, O., et al. 2022, *ApJS*, 258, 11, doi: [10.3847/1538-4365/ac3078](https://doi.org/10.3847/1538-4365/ac3078)
- Weibel, A., Oesch, P. A., Barrufet, L., et al. 2024, *MNRAS*, 533, 1808, doi: [10.1093/mnras/stae1891](https://doi.org/10.1093/mnras/stae1891)
- Williams, C. C., Oesch, P. A., Weibel, A., et al. 2025, *ApJ*, 979, 140, doi: [10.3847/1538-4357/ad97bc](https://doi.org/10.3847/1538-4357/ad97bc)
- Wright, A. H., Hildebrandt, H., van den Busch, J. L., & Heymans, C. 2020, *A&A*, 637, A100, doi: [10.1051/0004-6361/201936782](https://doi.org/10.1051/0004-6361/201936782)
- Yamaguchi, Y., Kohno, K., Hatsukade, B., et al. 2019, *ApJ*, 878, 73, doi: [10.3847/1538-4357/ab0d22](https://doi.org/10.3847/1538-4357/ab0d22)
- Yang, G., Caputi, K. I., Papovich, C., et al. 2023, *ApJL*, 950, L5, doi: [10.3847/2041-8213/acd639](https://doi.org/10.3847/2041-8213/acd639)
- Zaidi, K., Marchesini, D., Papovich, C., et al. 2024, *ApJ*, 969, 84, doi: [10.3847/1538-4357/ad45fa](https://doi.org/10.3847/1538-4357/ad45fa)

APPENDIX

A. CONTENT OF DATA RELEASE

The first data release of ULTIMATE deblending includes two catalogs for each field. The first catalog lists the basic information of source detection and the results of multi-wavelength photometry. The parameters listed in this catalog are shown in Table 3. The second catalog (Table 4) lists the redshifts and physical properties obtained from SED fitting.

Table 3. Parameters listed in the photometric catalog

Name	Units	Description
ID		Identifier of the JWST-detected sources
RA	deg	Right ascension
Dec	deg	Declination
X_image	pixel	Positions in JWST/NIRCam mosaics
Y_image	pixel	Positions in JWST/NIRCam mosaics
A_image	pixel ^a	Profile RMS along major axis
B_image	pixel	Profile RMS along minor axis
THETA_IMAGE	deg	Position angle (CCW/x)
KRON_RADIUS		Kron apertures in units of A and B
CLASS_STAR		S/G classifier output from source-extractor
flag_sextractor		Flags given by source-extractor
flag_kron		1: Kron apertures considered as unreliable; 0: Normal (see Section 3.3)
flag_TPHOT		> 0: TPHOT photometry are unreliable; 0: Normal (see Section 3.4)
flux_F444W_0.4/0.2		Ratio of uncorrected F444W flux densities in apertures with $d = 0.4''$ and $d = 0.2''$ ^b
flux_Band_tphot	μJy	Total flux densities in the low-resolution band “Band” ^c fitted by TPHOT
fluxerr_Band_tphot	μJy	Corrected flux density uncertainties in the low-resolution band “Band”
flux_Band_aper0.2	μJy	Flux densities in circular aperture ($d = 0.2''$) with aperture corrections in the band “Band”
fluxerr_Band_aper0.2	μJy	Corrected flux density uncertainties in circular aperture ($d = 0.2''$) in the band “Band”
flux_Band_aper0.3	μJy	Flux densities in circular aperture ($d = 0.3''$) with aperture corrections in the band “Band”
fluxerr_Band_aper0.3	μJy	Corrected flux density uncertainties in circular aperture ($d = 0.3''$) in the band “Band”
flux_Band_aper0.4	μJy	Flux densities in circular aperture ($d = 0.4''$) with aperture corrections in the band “Band”
fluxerr_Band_aper0.4	μJy	Corrected flux density uncertainties in circular aperture ($d = 0.4''$) in the band “Band”
flux_Band_aper0.5	μJy	Flux densities in circular aperture ($d = 0.5''$) with aperture corrections in the band “Band”
fluxerr_Band_aper0.5	μJy	Corrected flux density uncertainties in circular aperture ($d = 0.5''$) in the band “Band”
flux_Band_aper0.7	μJy	Flux densities in circular aperture ($d = 0.7''$) with aperture corrections in the band “Band”
fluxerr_Band_aper0.7	μJy	Corrected flux density uncertainties in circular aperture ($d = 0.7''$) in the band “Band”
flux_Band_aper1.0	μJy	Flux densities in circular aperture ($d = 1.0''$) with aperture corrections in the band “Band”
fluxerr_Band_aper1.0	μJy	Corrected flux density uncertainties in circular aperture ($d = 1.0''$) in the band “Band”
flux_Band_kron	μJy	Flux densities in Kron aperture ($k = 2.5$) with aperture corrections in the band “Band”
fluxerr_Band_kron	μJy	Corrected flux density uncertainties in Kron aperture ($k = 2.5$) in the band “Band”
flux_Band_best	μJy	The best estimated total flux densities in the band “Band”
fluxerr_Band_best	μJy	Uncertainties of the best estimated total flux densities in the band “Band”

NOTE. — (a) Pixel scale is 0.04 arcseconds. (b) Following I. Labbe et al. (2025), sources with $\text{flux_F444W_0.4/0.2} < 1.7$ can be considered as compact sources. (c) “Band” is the name of each band listed in Table 1.

Table 4. Parameters listed in the physical catalog

Name	Units	Description
ID		Identifier of the JWST-detected sources
RA	deg	Right ascension
Dec	deg	Declination
zphot		Photometric redshift fitted by Eazy
zspec		Spectroscopic redshift (see Section 4.1)
zspec_ref		Description of the spectroscopic redshift
zbest ^a		The redshift used to obtain the following parameters
delayed:age_16	Gyr	the 16th percentile (lower limit) of time since star formation began
delayed:age_50	Gyr	the 50th percentile (best estimation) of time since star formation began
delayed:age_84	Gyr	the 84th percentile (upper limit) of time since star formation began
delayed:tau_16	Gyr	the 16th percentile of the timescale of the delayed star-formation history
delayed:tau_50	Gyr	the 50th percentile of the timescale of the delayed star-formation history
delayed:tau_84	Gyr	the 84th percentile of the timescale of the delayed star-formation history
dust:Av_16	magnitude	the 16th percentile of the global absolute attenuation in the V band
dust:Av_50	magnitude	the 50th percentile of the global absolute attenuation in the V band
dust:Av_84	magnitude	the 84th percentile of the global absolute attenuation in the V band
dust:Av,b_16	magnitude	the 16th percentile of the Av for stars in birth clouds
dust:Av,b_50	magnitude	the 50th percentile of the Av for stars in birth clouds
dust:Av,b_84	magnitude	the 84th percentile of the Av for stars in birth clouds
stellar_mass_16		the 16th percentile of the log of the stellar mass (in M_{\odot} unit)
stellar_mass_50		the 50th percentile of the log of the stellar mass (in M_{\odot} unit)
stellar_mass_84		the 84th percentile of the log of the stellar mass (in M_{\odot} unit)
sfr_16	$M_{\odot} \text{ yr}^{-1}$	the 16th percentile of the star-formation rate
sfr_50	$M_{\odot} \text{ yr}^{-1}$	the 50th percentile of the star-formation rate
sfr_84	$M_{\odot} \text{ yr}^{-1}$	the 84th percentile of the star-formation rate
UV_colour_16		the 16th percentile of the rest-frame U-V color
UV_colour_50		the 50th percentile of the rest-frame U-V color
UV_colour_84		the 84th percentile of the rest-frame U-V color
VJ_colour_16		the 16th percentile of the rest-frame V-J color
VJ_colour_50		the 50th percentile of the rest-frame V-J color
VJ_colour_84		the 84th percentile of the rest-frame V-J color

NOTE. — (a) When the spectroscopic redshift is available, zbest = zspec, otherwise zbest = zphot.